

TOPICAL REVIEW

Magnetic x-ray microdiffraction

Paul G Evans¹ and Eric D Isaacs^{2,3}¹ Computer-Aided Engineering Center, University of Wisconsin, Madison, WI 53706, USA² Center for Nanoscale Materials, Argonne National Laboratory, Argonne, IL 60439, USA³ University of Chicago, Chicago, IL 60637, USAE-mail: evans@engr.wisc.edu

Received 8 February 2006

Published 21 July 2006

Online at stacks.iop.org/JPhysD/39/R245**Abstract**

Magnetic x-ray microdiffraction uses the structural specificity of x-ray diffraction to probe complex magnetic structures at the length scales relevant to physical phenomena including domain dynamics and phase transitions. Conventional magnetic crystallography techniques such as neutron or x-ray diffraction lack this spatial resolution. The combination of both reciprocal space and real space resolution with a rich magnetic cross section allows new microscopy techniques to be developed and applied to magnetism at the scale of single domains. Potential applications include a wide range of magnetic problems in nanomagnetism, the interaction of strain, polarization and magnetization in complex oxides and spatially resolved studies of magnetic phase transitions. We present the physical basis for x-ray microdiffraction and magnetic scattering processes, review microdiffraction domain imaging techniques in antiferromagnetic and ferromagnetic materials and discuss potential directions for studies.

(Some figures in this article are in colour only in the electronic version)

1. Introduction

Magnetism is connected to some of the most important problems in condensed matter physics, electronics and nanotechnology. New experimental techniques are necessary to address these problems. A wide range of fundamental questions become important as the frontiers of the technological manipulation and understanding of magnetic materials rapidly progress towards short time- and length-scales. Scientifically, the physics of magnetic complex oxide materials, including copper and manganese oxides, among others, is tied to the diverse set of magnetic phases of these materials. Superconductivity, ferroelectricity, insulating and conducting phases and long range electronic order all compete and cooperate with magnetism on a range of length and time scales. The details of this relationship, in particular the role of inhomogeneity, remain among the most exciting areas of the physical sciences.

The technological importance of magnetic materials arises from the potential to control the magnetic state of a material, including the magnetism of ions, the spin of the conduction

electrons and nuclei, and to subsequently interact with it. Magnetism has long been the basis for data storage and optical devices and is envisioned for a wide range of quantum mechanical devices based on the coherent manipulation of magnetism at nanometre lengths and short times. In data storage, for example, the rapid pace of innovation has already led to the manipulation of the magnetic states of materials over times of tens of nanoseconds and areas of approximately $1\ \mu\text{m} \times 1\ \mu\text{m}$ [1]. Data storage devices are rapidly integrating advanced magnetic materials with properties and magnetic structures that are controlled on the scale of nanometres. The development of devices manipulating currents of spins promises a potential route to quantum computing and high figure-of-merit bulk magnetic materials for applications in energy and optics.

Along with these scientific and technical challenges, magnetic structural and microscopy techniques have evolved to address the fundamental physics of magnetic materials. Magnetic structural techniques, for example, neutron scattering and bulk magnetization measurements, conventionally average over large volumes of magnetic materials and over long times.

In neutron diffraction experiments, Bragg diffraction and the dependence of the scattering cross section on the magnetism of the sample are used to determine the arrangement of magnetic moments. This has traditionally been the most important approach in understanding complex magnetic structures [2]. Despite recent advances in neutron optics and sources [3, 4], magnetic neutron diffraction can probe only large areas of material, on the order of at least square millimetres. In future neutrons sources, 50 μm resolution will be possible, but this is still far from the ultimate limits possible at 3rd and 4th generation x-ray sources.

Magnetic microscopy techniques include magneto-optic optical microscopy, magnetic force microscopy, spin polarized scanning tunnelling microscopy (STM) and flux decoration. Scanning probe techniques are based either on local measurements of the field outside a solid, as with magnetic force microscopy, or on tunnelling measurements of the momentum-integrated electronic density of states. Optical probes are limited to spatial resolutions of approximately the wavelength of light and can also depend on the dielectric constant or conductivity of the medium being probed. Several additional techniques-based x-ray absorption dichroism will be discussed below [5]. Traditional microscopy techniques do not convey the full degree of magnetic information that is necessary to understand magnetic materials at small scales.

Magnetic x-ray microdiffraction provides a new contrast mechanism based on magnetic structure rather than on magnetization. X-ray scattering includes the direction and magnitude of momentum transfer due to Bragg diffraction, a combination of reciprocal space and real space resolution important for understanding complex magnetic structures at small scales and in understanding how the local structure of the material couples to magnetism. X-ray microdiffraction techniques combine this Bragg diffraction approach with the capability of modern hard x-ray microscopy techniques to probe small volumes. The sensitivity of magnetic x-ray diffraction to magnetic structures is similar to that of conventional magnetic neutron scattering techniques based on interpreting the intensity and location in the reciprocal space of magnetic Bragg reflections.

The cross sections for magnetic x-ray scattering carry information about the local magnetic structure. These cross sections can be greatly enhanced at x-ray absorption edges by the dependence of the final state density of states in the absorption process on the magnetization. The x-ray energy can be tuned to absorption energy of specific elements distinguishing the contributions of different ions to the overall magnetic structure of the material.

The traditional strengths of x-ray scattering include the ability to probe materials in extreme environments: at low temperature, in high magnetic or electric fields, at high pressure or in buried layers. These strengths can carry over to sub-100 nm scale experiments with new developments in x-ray optics. New frontiers of x-ray diffraction are being steadily adapted as the basis for new magnetic microscopies. The combination of emerging structural magnetic microscopy techniques with the potential of synchrotron sources to produce picosecond-scale short x-ray pulses will lead to novel tools for magnetic dynamics [6, 7].

The ability to use the same probes used to understand the magnetic structure of materials as contrast mechanisms for

microscopy is important in understanding magnetic domains. These domains often dominate the magnetic and electronic properties at scales larger than a few micrometres. The sensitivity of magnetic x-ray diffraction to specific magnetic structures is important in materials such as Cr, MnO and CoO where there are several *types* of magnetic domains. In MnO and Cr the scattering wavevector allows the direction of the antiferromagnetic arrangement to be separated from the polarization of the spins participating in it. Magnetic structures can have a great diversity in the arrangement of spins

Microdiffraction techniques allow a new series of microscopy techniques to be developed which are based on a variety of magnetic contrast mechanisms. In this paper, we review the physical origin of magnetic x-ray scattering, discuss physics of focused x-ray techniques and review the magnetic microdiffraction experiments that have already been performed.

2. Magnetic x-ray scattering

The basic interactions leading to elastic magnetic x-ray scattering form the basis for magnetic x-ray microdiffraction. Magnetic scattering can result either from the non-resonant relativistic interaction of the photon with magnetic moments or from the electronic multipole atomic transitions associated with resonant scattering. Both resonant and non-resonant magnetic scattering mechanisms can be used in x-ray microdiffraction experiments. Texts [8, 9] and review papers [10, 11] provide the history of magnetic scattering and connect resonant magnetic scattering to the broader study of resonant interactions between x-ray photons and condensed matter.

2.1. Non-resonant magnetic scattering

The structural x-ray reflections of crystalline lattices arise due to Thomson scattering, which can be described quantitatively in the limit of low photon energies using classical mechanics. The acceleration of the electron by the electric field of the incident electromagnetic wave leads to electric dipole radiation (figure 1(a)). The Thomson scattering cross section depends only on the classical radius of the electron r_0 and on the direction of the scattered radiation relative to the plane in which the incident beam is polarized. Thomson scattering can also be derived using quantum mechanics, where it appears as the first term in an expansion of the operator $\vec{A} \cdot \vec{p}$. Here \vec{A} is the classical magnetic vector potential associated with the incident electromagnetic wave and \vec{p} is the momentum of the electron.

In both the classical and quantum-mechanical descriptions of Thomson scattering the spin of the electron and the finite energy and momentum of the x-ray photon are neglected. The scattering cross section becomes much more interesting when the most important classical or quantum mechanical effects taking the electron spin and photon energy into account are included. The first fully relativistic treatment of photon scattering was described in 1929 in the Klein–Nishina formulation of the Compton scattering cross-section [12]. Most importantly, when relativistic effects are included, terms coupling to the spin and orbital angular momentum of the electron appear in the cross section. Starting in the 1970s theoretical and experimental studies based on this

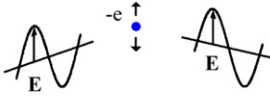
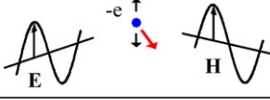


Force		Radiation
$-e\mathbf{E}$		electric dipole Thomson scattering
$-e\mathbf{E}$		magnetic quadrupole
$\nabla(\boldsymbol{\mu} \cdot \mathbf{H})$		electric dipole
$\mathbf{H} \times \boldsymbol{\mu}$		magnetic dipole

Figure 1. The acceleration of an electron by the electric field of the incident field leads to electric dipole radiation (top panel). Other classical electrodynamic scattering processes depend on the spin of the electron.

insight showed that x-rays could be scattered not only by the distribution of charges but also by the magnetic order within a material [13–16]. Including the magnetic interactions produced a series of terms in the cross section proportional to powers of $\hbar\omega/mc^2$, where $\hbar\omega$ is the energy of the x-ray photon, m is the mass of the electron and c is the speed of light.

Although the series of quantum mechanical extensions of the Thomson scattering process are inherently quantum mechanical [15], the interactions leading to magnetic scattering also have analogues in classical mechanics that can be used to provide an intuitive understanding of the scattering process. These can provide an intuitive picture of the magnetic scattering picture equivalent to the classical description of Thomson scattering. The classical scattering processes are illustrated in figure 1 [17, 18]. One process leading to photon scattering by the spin of an isolated electron, for example, is the acceleration of the electron by the electric field of the incident wave and magnetic dipole radiation by the moving magnetic moment of the electron [17, 18]. Magnetic dipole radiation is weaker than electric dipole radiation by the same factor of $\hbar\omega/mc^2$ that appears in the quantum mechanical expansion [14].

The generalization from the scattering from a single magnetic moment to the diffraction patterns of magnetic solids is built up from the fundamental amplitude of the interaction in the same way that the description of x-ray scattering purely from charge begins with Thomson scattering and introduces atomic scattering factors and finally structure functions (for example, [19]). This potential to use the well-known physics of diffraction allows the magnetic interaction to be used as quantitative probes for magnetism in both scattering and diffraction. Extended structures can be described using magnetic structure functions, and the magnetic reflections will thus have the same structural sensitivity as the charged reflections. Even with the large enhancements at absorption resonances, magnetic reflections are orders of magnitude weaker than structural x-ray reflections, so the kinematic limit of x-ray scattering is almost always used. At charge–magnetic interference reflections, with effectively perfect crystals it

may be necessary to use dynamical scattering to interpret the intensity of reflections.

The magnetic scattering factor is a tensor relating the amplitudes of the two polarizations of the scattered radiation to the amplitudes of the incident waves. The scattering factor depends on the incident and diffracted beam wavevectors \mathbf{k} and \mathbf{k}' and $\mathbf{S}(\mathbf{Q})$ and $\mathbf{L}(\mathbf{Q})$, the Fourier transforms of the spin and orbital magnetic moments, respectively, with $\mathbf{Q} = \mathbf{k}' - \mathbf{k}$. The magnetic contribution of non-resonant scattering to the scattering factor is [16, 20]

$$f_{\text{non-res.}}^{(\text{mag})} = ir_0 \frac{\hbar\omega}{mc^2} f_D \left[\frac{1}{2} \mathbf{L}(\mathbf{Q}) \cdot \mathbf{A} + \mathbf{S}(\mathbf{Q}) \cdot \mathbf{B} \right]. \quad (1)$$

Here the unitless matrices \mathbf{A} and \mathbf{B} describe the polarization and energy dependence of the magnetic interaction. The Debye–Waller factor f_D is included in equation (1) to account for the effect of thermally excited perturbations of the atomic order on magnetic scattering. The matrices \mathbf{A} and \mathbf{B} depend on the polarizations of the incident and scattered beams, $\hat{\mathbf{e}}$ and $\hat{\mathbf{e}}'$, respectively [16]:

$$\begin{aligned} \mathbf{A} &= 2(1 - \hat{\mathbf{k}} \cdot \hat{\mathbf{k}}')(\hat{\mathbf{e}}' \times \hat{\mathbf{e}}) - (\hat{\mathbf{k}} \times \hat{\mathbf{e}})(\hat{\mathbf{k}}' \cdot \hat{\mathbf{e}}') + (\hat{\mathbf{k}}' \times \hat{\mathbf{e}}')(\hat{\mathbf{k}} \cdot \hat{\mathbf{e}}), \\ \mathbf{B} &= (\hat{\mathbf{e}}' \times \hat{\mathbf{e}}) + (\hat{\mathbf{k}}' \times \hat{\mathbf{e}}')(\hat{\mathbf{k}} \cdot \hat{\mathbf{e}}) - (\hat{\mathbf{k}} \times \hat{\mathbf{e}})(\hat{\mathbf{k}}' \cdot \hat{\mathbf{e}}') \\ &\quad - (\hat{\mathbf{k}}' \times \hat{\mathbf{e}}') \cdot (\hat{\mathbf{k}} \times \hat{\mathbf{e}}). \end{aligned} \quad (2)$$

The conventional Thomson scattering cross section f_0 can be written in terms of the same quantities. This form is useful in understanding the potential for cross terms between charged and magnetic scattering:

$$f_0 = \rho(\mathbf{Q})r_0(\hat{\mathbf{e}}' \cdot \hat{\mathbf{e}}). \quad (3)$$

The total non-resonant scattering factor for a magnetic ion is the sum of the conventional Thomson scattering, the anomalous scattering correction $f' + if''$ and the magnetic contribution $f_{\text{non-res.}}^{(\text{mag})}$ [20],

$$f = f_0 + f' + if'' + f_{\text{non-res.}}^{(\text{mag})}. \quad (4)$$

An estimate of the relative intensities of reflections arising from non-resonant magnetic scattering and Thomson scattering can be obtained using equation (4). The amplitude due to magnetic scattering depends on the value of the perturbation expansion factor $\hbar\omega/mc^2$, and the intensity is proportional to this factor squared. At the typical x-ray photon energies of diffraction experiments $(\hbar\omega/mc^2)^2$ is on the order of 10^{-4} . The intensity of magnetic Bragg reflections is an even smaller fraction of the intensity of structural reflections arising purely from Thomson scattering. This factor depends on the value of the structure function for each charged Bragg reflection. All core electrons contribute to charged scattering, but only a small fraction of the total number of electron spins lead to a net magnetization. In antiferromagnetic MnF_2 , for example, the ordered magnetic moment in the antiferromagnetic lattice corresponds to on the order of 1 electron out of a unit cell consisting of 48 electrons [21]. The non-resonant magnetic Bragg reflection in MnF_2 is thus a factor of 10^8 smaller than the structural reflections arising from Thomson scattering. A similarly large ratio applies to non-resonant magnetic x-ray reflections from other materials. This intensity difference effectively limits studies of non-resonant magnetic scattering to synchrotron sources

where diffraction experiments can have sufficient dynamic range to study magnetic reflections.

The polarization and incident wavevector dependence of the magnetic scattering cross section can be used to probe the structure and spin polarization of magnetic structures. Because the interactions leading to non-resonant magnetic x-ray scattering are extremely well-known, non-resonant scattering has proved to be an excellent tool for confirming the relative contributions of spin and orbital magnetic moments to the total magnetization. Non-resonant scattering is useful when the resonant enhancement is small, as for K edges of transition metals [22].

As predicted in early theoretical work, non-resonant magnetic scattering is most easily observed in systems in which the reciprocal lattice of the magnetic structure is distinct from the reciprocal lattice of the atomic cores. The strong Bragg reflections from the atomic lattice are then far in reciprocal space from the weak magnetic reflections. Non-resonant scattering has the advantage of being quantitatively described by calculations. The cross sections predicted on the basis of spin form factors $S(\mathbf{Q})$ and the quantum mechanical scattering cross section have been verified experimentally to a high degree of accuracy [21].

Magnetic structures of several types have been studied with non-resonant magnetic x-ray scattering, including the helical antiferromagnet Ho [23, 24], ferrimagnets and antiferromagnets such as Cr [25] and MnF₂ [21]. Under some conditions, magnetic diffraction from ferromagnetic materials can be observed using the interference between Thomson scattering and non-resonant magnetic scattering, such as in ferromagnetic Fe [26, 27].

2.2. Resonant magnetic scattering

The magnetization of solids often results from a net magnetic polarization of electronic states at or near the Fermi level, and thus the spin-dependent density of empty states. At the appropriate photon energies, these empty states can serve as the final states for x-ray absorption, yielding to a dichroism, or polarization dependence, in the absorption spectrum [28, 29]. The states are also intermediate states in the quantum mechanical description of resonant scattering, leading to resonant cross sections that depend on the spin polarization of states near the Fermi level [20].

Resonant scattering results in additional magnetic terms in the scattering factor. A quantum mechanical description of the absorption process can be derived based on a perturbation expansion of contributions to the scattering factor from dipole and quadrupole transitions. The role of these transitions was included in the early theoretical studies of magnetic scattering [15, 16, 30]. The most general magnetic resonant scattering factor for electric multipole transitions depends on the geometrical and angular overlap of initial, intermediate and final states [20, 30],

$$f_{EL}^e(\omega) = \frac{4\pi}{k} f_D \sum_{M=-L}^L [\hat{\epsilon}'^* \cdot \mathbf{Y}_{LM}^{(e)}(\hat{\mathbf{k}}) \mathbf{Y}_{LM}^{(e)*}(\hat{\mathbf{k}}) \cdot \hat{\epsilon}] F_{LM}^{(e)}(\omega). \quad (5)$$

Here, the factors $\mathbf{Y}_{LM}^{(e)}(\hat{\mathbf{k}})$ are the vector spherical harmonics and the factor $F_{LM}^{(e)}(\omega)$ determines the strength of the resonant

enhancement. For dipole transitions, which have $L = 1$, the resonant scattering factor becomes

$$f_{nE1}^{\text{XRES}} = (\hat{\epsilon}' \cdot \hat{\epsilon}) F^{(0)} - i(\hat{\epsilon}' \times \hat{\epsilon}) \cdot \hat{\mathbf{z}}_n F^{(1)} + (\hat{\epsilon}' \cdot \hat{\mathbf{z}}_n)(\hat{\epsilon} \cdot \hat{\mathbf{z}}_n) F^{(2)}. \quad (6)$$

The term containing $F^{(0)}$ gives rise to anomalous charge diffraction but does not depend on the magnetization of the material. The remaining two terms depend on the direction of the magnetization (axis of quantization) at the n th ion, $\hat{\mathbf{z}}_n$, and the quantum mechanical factors, $F^{(1)}$ and $F^{(2)}$. $F^{(1)}$ and $F^{(2)}$ depend on the photon energy and the atomic energy level structure of the resonant ion. Higher order transitions, including electric quadrupole and magnetic dipoles, can be important when the resonant effects due to dipole transitions are small [31].

Magnetic scattering can result in purely magnetic peaks arising from the square magnitude of the magnetic structure factor alone or as an interference term in which the magnetic and charge terms of the scattering factor appear as a cross-product. The cross section for pure magnetic scattering applies when the magnetic reflections are isolated from charged reflections in reciprocal space, as in incommensurate antiferromagnets or commensurate magnetic structures in which the Bragg peak of the lattice is forbidden by the crystallographic symmetry. For ferromagnetic materials the dominant source of magnetic scattering at Bragg reflections is this interference between charged and magnetic interactions. Understanding both the magnetic and electronic contributions to resonant scattering can require a significant theoretical effort and remains an important priority for the magnetic scattering community.

There is useful magnetic information contained in the terms of the magnetic x-ray factors which are proportional to the degree of circular polarization of the incident x-ray beam. The reversal of this polarization can thus isolate a specific magnetic contribution to the signal. The magnetic scattering cross sections can also be quantitatively interpreted to find the direction of the magnetization locally. For ferromagnetic materials, the most useful resonant dichroism effects are often observed with circularly polarized incident x-ray photons. The helicity of the x-ray photons requires that dipole transitions occur with a net change in the angular momentum of the electron during the excitation to the virtual state resulting in a dichroism that is strongest with highly spin-polarized states.

Among the important elements present in relevant magnetic solids, the hard x-ray spectrum includes the K edge absorption resonances of transition metals, the L edges of rare earths and the M edges of actinides. Many of these resonances have been extensively explored in both theoretical and experimental studies, providing a firm basis for the interpretation of resonant diffraction results [32]. The L and M edges magnetic materials having large resonant dichroisms are commonly used in x-ray magnetic studies of rare earth materials [33]. The M edges of actinide elements can have enhancement factors of 10^7 or more [34].

The K -edges of magnetic transition metals, which were the first resonances to be studied [35], have weakly polarized final states and exhibit a small dichroism, as small as 0.1% or even less [32]. These dichroisms are tiny compared with the 1% or more found in L edges of rare earths.

In elemental Cr, for example, the resonant enhancement makes a negligible contribution to the intensity of the stronger of the two channels of non-resonant magnetic scattering [25] and leads to an enhancement of only approximately 2 intensity in the polarization-rotating channel [36].

In many transition metal ions, the spin magnetic moment is the dominant contribution to the total magnetization. The spin polarization still results in small perturbations in the empty intermediate states of resonant scattering, but these effects are small in comparison with the effects of orbital moments. In materials with primarily spin magnetic moments, the relative importance of resonant scattering is thus reduced in comparison with non-resonant scattering. Theoretical studies of resonant scattering are crucially important for these materials and can show good agreement with experimental results [37–40].

3. X-ray microscopy and microdiffraction

X-ray microscopy uses the unique and diverse interactions of x-ray photons with materials to provide information that complements other microscopy techniques. There are three primary and complementary approaches to x-ray microscopy: full field microscopy, scanning x-ray probes and lenseless coherent scattering. Full-field x-ray microscopy records the intensity of a transmitted or reflected x-ray as a function of real-space position. This approach is useful in transmission imaging, in which images have absorption contrast similar to a medical radiograph and in forming images using Bragg reflections. A second important contrast mechanism in full-field microscopy relies on phase shifts in the transmitted x-ray beam. Phase contrast imaging is exceptionally sensitive to density variations in materials. Full-field images can be acquired directly on an imaging detector [41].

Scanning x-ray probe microscopy uses the highly local and quantitative interaction of x-rays with materials to form images based on studying single small regions one at a time. As in the full-field microscopies, the basic interaction leading to contrast can be absorption alone or scattering, as in the case of microdiffraction. Microdiffraction uses the scanned probe beam to excite Bragg reflections from well-defined small volumes. As we show below, these reflections from spatially isolated areas can be used to form images and as a structural and magnetic probe.

The third important approach to microscopy is to interpret the speckle pattern arising from coherent scattering. Lensless coherent microscopy can have excellent spatial resolution, limited in principle by the experimental capability to measure intensities accurately across large volumes of reciprocal space. The limited dynamic range of detectors and incoherent and inelastic processes will pose problems for hard x-ray magnetic analogues of this technique.

3.1. X-ray nanofocusing techniques

X-rays are fundamentally more difficult to focus than visible light because the real part of the index of refraction is close to unity in solids. This weak interaction leads to relatively small phase shifts in optical elements and, in turn, results in long focal lengths for diffractive or refractive optics. In return,

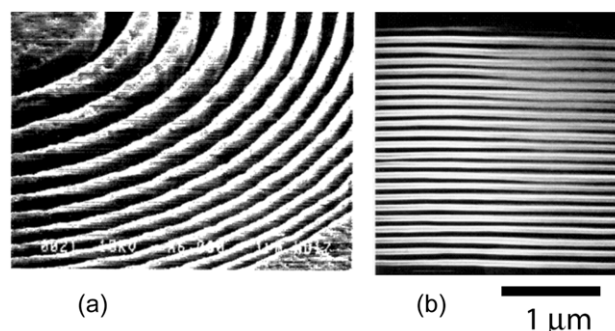


Figure 2. Fresnel phase zone plates. In the diffraction limit, the focal spot size is set by the width of the outermost zone. Rapid progress has resulted in a decrease in the width of this feature from (a) $0.5\ \mu\text{m}$ in 1992, after [47] to (b) better than $50\ \text{nm}$ presently, after [48].

due to this weak interaction, the scattering and absorption processes can be described quantitatively, which in turn allows the contrast observed in microscopy techniques to be interpreted accurately. Strategies for producing tightly focused x-ray spots have been based on using an x-ray optical element to produce a demagnified image of either the x-ray source or a spatially-filtered secondary source. The focused beams are factors of 10^5 to 10^6 more intense than the intensity that would fall on the focal spot due to an unfocused beam. These large gains result in tightly focused monochromatic x-ray beams, a total flux of photons that is on the order of 10^{10} per second in an energy bandwidth of 0.1% for zone plate optics. These intensities are sufficient for a wide variety of magnetic scattering experiments.

The most important sources of x-rays for microdiffraction experiments with high spatial resolution are third-generation electron storage ring light sources. These third-generation sources are optimized to produce synchrotron radiation using undulator insertion devices, leading to beams with orders of magnitude higher brilliance than previous facilities. For hard x-rays, with third-generation light sources, the sources are small enough, on the order of a few microns in the vertical direction, that modest focal lengths can produce a demagnification of a factor of several hundred and a focused beam far below $100\ \text{nm}$ in diameter. Focusing optics can easily be combined with schemes for creating circularly polarized x-ray photons such as transmission crystal phase plates [42–45].

The most common focusing optical elements for hard x-ray microscopy are Fresnel zone plates (figure 2) [46–48], and Kirkpatrick–Baez mirrors (figure 3(a)) [49]. Other emerging x-ray focusing schemes include bulk and microfabricated lenses [50, 51], compound refractive lenses (figure 3(b)) [52], linear zone plates [53] and hybrid combinations of these approaches such as Bragg–Fresnel optics [54] and multilayer volume gratings [55]. There has recently been a rapid improvement in the focal spot size and intensity of focused beams using each of these optical approaches. Spot sizes as small as $50\ \text{nm}$ have been demonstrated for zone plates, mirrors and compound lenses [56–62].

Theoretical and experimental studies have shown that focal spot sizes of approximately $5\ \text{nm}$ can be achieved in principle. The ultimate resolution of x-ray focusing optics is limited by both the wavelength of the x-rays and the numerical

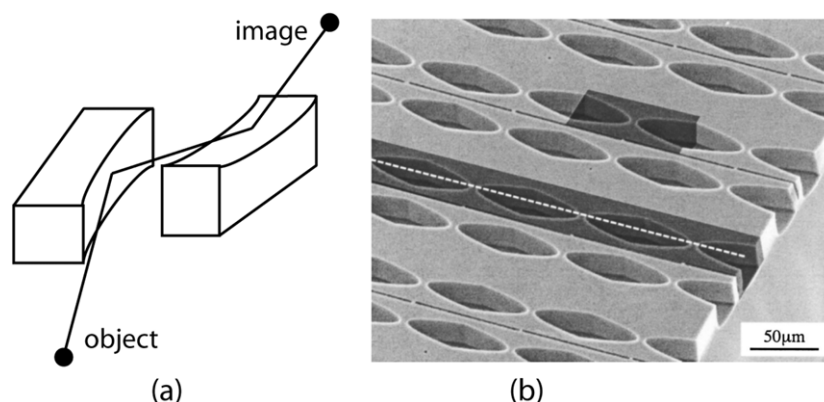


Figure 3. (a) Kirkpatrick–Baez x-ray mirrors, after [47]. (b) Lithographically defined compound refractive lenses, after [65].

aperture (NA) of the optic. The focal spot size or resolution is given by $0.6 \lambda/\text{NA}$ full width-at-half maximum (FWHM). Due to the rather small deflection of x-rays by matter, the largest NA presently achievable is on the order of 10^{-3} . It was recognized in the original 1948 publication of Kirkpatrick and Baez that mirrors have a NA limited by the critical angle for external reflection. The energy dependence of the critical angle cancels the factor of λ in the resolution estimate so that the ultimate resolution depends only on the density of the mirror coating. Focal spot sizes of 6 nm can be achieved in mirror structures with high-density optical coatings [49]. The ultimate limitations of zone plates and refractive lenses can also be found using similar physical arguments [55, 63–65]. For example, because all these optical elements involve illuminating a significant volume of material with x-ray light, the intensity of the focused beam is added to incoherently scattered background radiation, which effectively limits the ultimate size of the probe. For refractive lenses in particular, the forward scattered radiation due to Compton scattering provides one potential lower limit for spot sizes that can be estimated from first principles [63]. Assuming that the outermost zones of zone plates, figure errors of mirrors or refractive lens shapes can be optimized arbitrarily, subsequent limitations are predicted that limit focusing to spot sizes of a few to several nanometres [66]. Spot sizes at the single-digit nanometre scale are likely to occur as sources and optics continue to evolve.

Zone plates are the x-ray analogue of convex lenses that can be used to produce a magnified or demagnified image of the x-ray source. In microprobe experiments, with high enough demagnification and a suitably small source size, the focal spot produced by zone plate optics is set by the dimension of the outermost zone of the zone plate. The same effect sets the resolution in imaging experiments. A zone plate with outermost zone width Δr will produce a focused spot of size $1.22 \Delta r$, determined by the diameter of the first null in the Airy pattern [67]. This is also the spatial resolution according to the Rayleigh criterion. Often in experiments, the FWHM of the beam is measured instead of the position of the first null of the Airy pattern. Ideally, the FWHM resolution should be a factor 2.37 smaller than the Rayleigh criterion. In the absence of other effects a zone plate with an outermost zone width Δr can in principle produce a focused x-ray beam with an FWHM of $0.52 \Delta r$.

Zone plates are conventionally fabricated using nanolithography by creating a thin-film binary approximation to a true Fresnel zone plate [46, 47]. A critical challenge in producing x-ray zone plates is to produce outermost zones that are extremely narrow and simultaneously tall enough to produce the necessary phase shift in the transmitted x-ray beam. The phase difference accumulated between the ray transmitted by the material of the zone plate and the ray passing through air in the empty zones is ideally π in order to maximize the x-rays deflected into the focal spot. The height-to-width aspect ratio that is achievable with today's technology is approximately 15 to 1 [68]. This results in a phase shift, $2\pi t\delta/\lambda$, between 0.05π and 0.5π . For example, with $\delta = 3 \times 10^{-5}$, as for 10 keV photons in Au, a high-resolution zone plate with 50 nm zones with $t = 750$ nm produces a phase shift of only 0.4π . The efficiency with which x-rays are concentrated to the first order focus of high resolution zone plates is thus approximately 10%, much less than the theoretical limit of $4/\pi^2 \approx 40\%$ for binary approximations to Fresnel lenses. Structures with greater lithographic complexity, including those with blazed zones, can have higher efficiency at the cost of a simultaneously larger focused spot size [69, 70]. Hard x-ray zone plates have evolved rapidly, progressing from $0.5 \mu\text{m}$ outermost zone widths in 1992 to less than 50 nm presently (figure 2).

The index difference between the air or vacuum ambient and solids is larger for soft x-rays optics, which produce smaller probe spot sizes than hard x-ray focusing devices and resolve smaller features in imaging experiments, as small as 15 nm at present [68].

Kirkpatrick and Baez originally described focusing x-rays using a crossed pair of mirrors in 1948 [49]. Each mirror focuses x-rays in only one dimension, so two mirrors focusing in orthogonal directions are necessary to produce a beam that is focused to a point (figure 3). Kirkpatrick–Baez mirrors are also useful in studies with a polychromatic x-ray beam, in which synchrotron radiation is not passed through a monochromator, because the focal length of mirror optics does not depend on the x-ray wavelength. Tightly focused polychromatic x-ray beams allow microdiffraction studies based on Laue diffraction [71, 72] or potentially on white-beam magnetic scattering techniques [26]. Mirrors also have the potential to quickly work back and forth between single-crystal and Laue diffraction methods [73, 74]. In comparison, the focal length of zone plates is proportional to the x-ray photon energy,

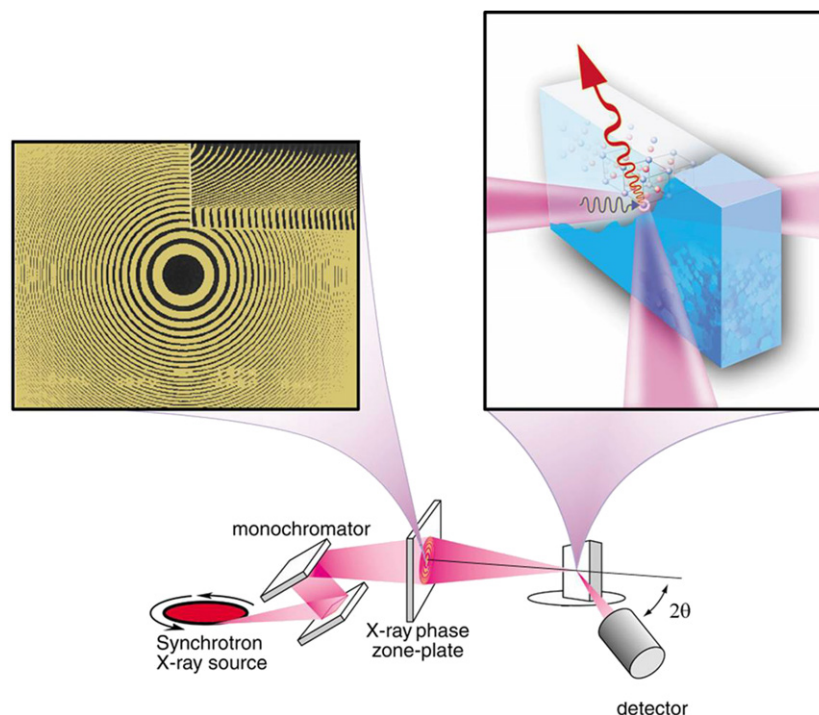


Figure 4. X-ray microdiffraction using Fresnel phase zone plate optics, after [75].

which effectively limits zone plate optics to experiments with monochromatic x-ray beams.

Mirrors and compound refractive lenses are also particularly important in focusing high-energy x-rays with energies of 25 keV or more because zone plates lose much of their efficiency at high photon energies. Because the deviation of the real part of the dielectric constant from unity decreases approximately as $1/\hbar\omega$, zone plates for high-energy x-rays become difficult to fabricate. While compound, or stacked, zone plates are possible, zone plates are optimal at intermediate x-ray energies.

3.2. Microdiffraction

Microdiffraction instruments based on zone-plate focusing optics offer both high spatial resolution and sufficient working distance to incorporate sample environments such as cryostats, high-pressure cells or furnaces. The ability of hard x-rays to take advantage of these types of environments will have an important role in broadening the range of phenomena that can be probed with magnetic microscopy. A schematic illustration of a microdiffraction instrument is shown in figure 4 [75, 76].

The reciprocal space resolution of microdiffraction is set by the same factors that determine the resolution of experiments with unfocused x-ray beams. In comparison with other synchrotron radiation methods, where the incident beam divergence is small, the large NA of microdiffraction optics can be a significant issue. At the very least, the widths and intensities of x-ray reflections are influenced by the beam divergence.

Focusing x-ray beams increases the intensity at the focal spot but also introduces appreciable beam divergence. At synchrotron sources the focused beam fills the direction-incident angle phase space very differently from conventional

diffraction experiments. Zone plate optics, for example, produce a well-defined cone of incident radiation that is highly monochromatic. The circular image of the zone plate minus a central disc occupied by the centre stop is effectively imprinted on the focused beam. This effect leads to a distribution of intensity in reciprocal space different from when the beam is both divergent and has a wide distribution of energies and initial positions. In particular, the scattering angle is well defined for each ray within the cone, which leads to a new set of challenges in quantitatively interpreting diffraction patterns. The possibility also exists to recover much more information by carefully analysing how the beam divergence contributes to the observed diffraction pattern.

X-ray diffraction from finite structures or with finite-size probes results in a broadening of Bragg reflections. In structures consisting of only N atomic planes or when only N planes are illuminated, the intensity profile in reciprocal space is proportional to $\text{Sin}^2(\pi N Q a)/\text{Sin}^2(\pi Q a)$, regardless of the interaction that leads to scattering. The widths of magnetic peaks are therefore set by the same finite size effects that set the widths of charged reflections. An estimate of the importance of the finite size effects in microdiffraction experiments can be found by comparing widths due to finite size effects with the divergence arising from the focusing optics. With a NA of 10^{-3} , as in present optical systems, the beam divergence is approximately 0.1° .

For a hypothetical study of a structure with a 4 \AA lattice constant at $Q = 0.5 \text{ \AA}^{-1}$, the width of the reflection due to the finite size effect exceeds the equivalent of 0.1° beam divergence for features, e.g. nanoparticle diameters, film thickness or magnetic domains sizes, smaller than 400 \AA . If the magnetic coherence lengths within magnetic structures do not reach this length scale the magnetic reflections will be broadened significantly, potentially even causing weak

magnetic reflections to overlap nearby stronger reflections. Thus the reciprocal space precision of experiments is limited by beam divergence introduced by the focusing optics for large structures and by the finite size effect for small structures, with a cross over at the scale of tens of nanometres or less.

3.3. Complementary soft x-ray techniques

Soft x-ray photons in the energy range from approximately 100 to 2 keV can have strong magnetic interactions with the L edges of transition metals and the M edges of rare earths. These strong interactions are the basis for element specific probes of magnetism based on scattering, imaging and spectroscopy. Conventionally, these techniques have been based on either spatially resolved or averaged studies of the circular dichroism of absorption edges or on scattering from an ensemble of domains [77]. The physical basis of both resonant scattering and dichroism experiments is based on the description given in section 2.

Soft x-rays photons have energies that are roughly one order of magnitude lower than hard x-ray photons and thus have insufficient momentum to reach reflections far from the origin in reciprocal space. In spite of this potential shortcoming, the development of soft x-ray scattering techniques has roughly paralleled the hard x-ray magnetic diffraction techniques. Magnetic scattering experiments have most often been reflectivity studies, which probe the magnetic signatures of the specular and diffuse reflections from a sample [78, 79]. The polarization and sample-magnetization dependence of the scattered radiation is a sensitive probe of nanometre-scale magnetic phenomena. In terms of the crystalline lattice, reflectivity and diffuse scattering experiments in this limit effectively use the (000) reflection, which carries no structural information about the crystalline or atomic-scale magnetic lattice.

Long-range magnetic order can lead to Bragg reflections that are sufficiently close to the origin of reciprocal space that they fall within the limited Q range accessible using soft x-rays. Even though soft x-rays lack sufficient momentum to reach Bragg reflections associated with the atomic periodicity, it was recently recognized that resonant Bragg diffraction using soft x-rays can be applied to long-wavelength phenomena [80, 81]. Abbamonte *et al* used the resonant enhancement of the Bragg reflection from a long-wavelength charge modulation to attribute its origin to an ordered arrangement of holes in the cuprate ladder layer [80]. This strategy can in principle be extended to long-period magnetic structures including the helices or spin density waves (SDWs) of figure 5. A further potential development would be to combine soft x-ray focusing and scattering techniques to take magnetic hard x-ray microdiffraction techniques to their extreme long-wavelength limit. The richness of L - and M -edges in the soft x-ray regime and the lack of other suitable microscopy techniques sensitive to long-wavelength magnetic modulations form an important niche for future long-wavelength resonant microdiffraction techniques.

A second important consequence of the long wavelength of soft x-rays is that high degrees of spatial coherence are more easily obtained in beams of soft x-rays than with hard x-rays [67]. Scattering with a coherent incident beam leads to speckle

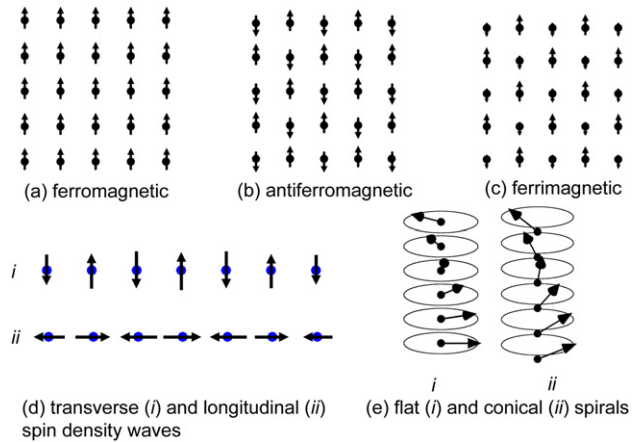


Figure 5. Magnetic structures include ferromagnetic, antiferromagnetic and ferrimagnetic arrangement of moments (a)–(c), transverse and longitudinal SDWs (d) and (e) flat and conical spirals.

patterns specific to a particular arrangement of scatterers rather than a more statistically averaged diffuse scattering pattern. The soft x-ray speckle pattern associated with the arrangement of domains in magnetic thin films can be acquired and inverted using phase-retrieval algorithms or holography to yield lensless full-field magnetic images [82, 83]. The speckle pattern can also be used without diffraction to study the wavevector dependent dynamics of fluctuations [84].

Magnetic domains can also be imaged using soft x-ray absorption alone. Magnetic information arising solely from the absorption cross section can also be obtained using images of the x-ray fluorescence, photoelectron emission or x-ray absorption as a function of position. X-ray magnetic circular dichroism, for example, can be used to form images of the magnetization of a material using photoelectrons, as in photoemission electron microscopy (PEEM) [85, 86], or in scanning microprobe of x-ray absorption images [74]. Dichroism arises from the influence of magnetism on the energy level spectrum at particular ions and is typically probed using light resonant with photons at atomic resonant absorption edges. These experiments can be designed to take advantage of the time structure of synchrotron radiation, allowing 100 ps scale resolution in measurements based both on absorption [87] and on photoelectron imaging [88].

3.4. Complementary microfluorescence techniques

Images of the x-ray fluorescence are essentially maps of the imaginary part of the resonant magnetic structure factor at $Q = 0$ and thus depend on the magnetic interactions described in section 2.2 [89]. Exactly as in the soft x-ray techniques, the circular dichroism of the fluorescence intensity provides an image of the magnetization. These techniques are the hard x-ray analogues of the transmission x-ray microscopy [85, 86] and photoelectron microscopy techniques (8) widely used with soft x-ray microscopes, in that the magnetic information arises solely from the magnetic cross section.

Pollman *et al* have demonstrated this microfluorescence approach in a SmCo/Co multilayer sample in which the hard x-rays enable the experiment to probe buried layers [90].

Cady *et al* have shown that microfluorescence images can be acquired at low temperatures [91]. These maps of the local resonant absorption can, in principle, complement microdiffraction studies because fluorescence weights the local magnetization vector differently from the scattered radiation. As with any other study of the dichroism alone, microfluorescence-based magnetization studies do not have the structural specificity of diffraction techniques.

4. Imaging antiferromagnetic and ferrimagnetic domains

4.1. Imaging modulation-direction and spin-polarization domains in Cr

Imaging techniques promise to revolutionize the study of magnetic phenomena in Cr and other antiferromagnets by connecting area-averaged transport and magnetic properties measurements to their fundamental origins at the microscopic scale. The fundamental role of disorder, for example, in the form of crystalline defects, magnetic impurities, or even microfabricated features, can be studied at both the local level through these emerging imaging techniques and at the statistical scale with large-scale, bulk probes such as transport and magnetic susceptibility. This brings about the potential to connect local nanomagnetic phenomena in antiferromagnets with long-standing hypotheses developed on the basis of a statistical population of domains. Transport and magnetic susceptibility measurements have recently suggested that Cr and its dilute alloys show hallmarks of quantum phase transitions, making these materials an ideal, controlled system to probe a number of predictions [92].

4.1.1. Complex magnetism of a simple metal. Elemental chromium is a body centred cubic metal, which despite its body centred cubic crystalline structure has surprisingly complex magnetic behavior [93]. The antiferromagnetism of elemental Cr has been linked to a wide variety of physical phenomena ranging from anomalous optical and mechanical properties to quantum magnetism in alloys [92]. Pure Cr is an antiferromagnet, with spins ordered in a long-range SDW. The magnetic phase transition at the Néel temperature T_N produces an energy gap across a large fraction of the Fermi surface, which effectively lowers the number of electrons that can participate in conduction. The reduction in Fermi surface area results in a famous anomaly in the resistivity [93]. An anisotropy in the conductivity as a function of the direction of the current relative to the antiferromagnetic ordering direction and spin polarization direction has also been inferred from transport measurements. This anisotropy is thought to be the source of the large $1/f$ noise observed in Cr with strong features near magnetic phase transitions.

The antiferromagnetic domains of elemental Cr can be visualized using several techniques. Spin polarized STM, for example, probes the domain structure in the atomic layer at the surface [94]. Structural STM studies can image the distortion associated with the strain wave in the surface layer [95]. Spin polarized scanning electron microscopy can image the magnetism not in the Cr directly but instead in ferromagnetic sensing layers deposited on the surface [22]. At larger

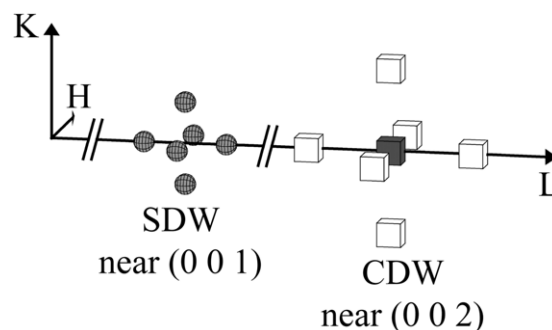


Figure 6. The reciprocal space of elemental Cr. Non-resonant magnetic x-ray scattering leads to superlattice SDW reflections (spheres) near the forbidden (001) Bragg reflection. A strain wave (CDW) arises from the SDW and produces x-ray reflections near (002) (cubes), after [99].

scales, neutron and x-ray topography have been used to study magnetic domains in Cr with millimetre resolutions and will be discussed briefly in the following section.

Despite this level of knowledge of the basic phenomena of the magnetism of chromium, a variety of fundamental questions are unanswered and many questions are answered only anecdotally. It is known, for example, that the strains associated with producing a surface of a single crystal are sufficient to force the crystal into a state in which only magnetic domains with magnetic ordering vector \mathbf{Q} pointing along the surface normal are present. The quantitative details of this anisotropy, and the response of the magnetism of Cr to strain, are poorly known.

The ordered magnetic moments in Cr are polarized transverse to the SDW wavevector at temperatures between the Néel transition at $T_N = 311$ K and a spin-flip transition at $T_{SF} = 123$ K [96,97]. At temperatures below T_{SF} the spins are polarized along the direction of the incommensurate SDW in a longitudinal phase. The direction \mathbf{Q} of the SDW propagation is always along one of the $\langle 001 \rangle$ directions of the cubic lattice. A microscopic volume of pure Cr may thus be in one of the three possible \mathbf{Q} domains at low temperatures below the spin-flip transition and in one of the six possible combinations of \mathbf{Q} and the spin polarization \mathbf{S} at temperatures between T_{SF} and T_N . The SDW also produces a distortion of the lattice leading to a strain wave with half the period of the SDW. This strain wave is often referred to as a charge density wave (CDW).

4.1.2. Magnetic x-ray scattering from Cr. The reciprocal space of a multi-domain Cr single crystal is shown in figure 6. Three pairs of incommensurate magnetic Bragg reflections appear near the (001) position of the reciprocal lattice of the Cr crystal. The (001) x-ray reflection is forbidden in the body centred cubic lattice, which leads to extremely low background at the SDW reflections. The six SDW spots are produced by the three possible \mathbf{Q} domains. The spots displaced along the H , K and L directions of reciprocal space from (001) belong to domains with \mathbf{Q} along $[100]$, $[010]$ and $[001]$, respectively. At low temperatures the period of the SDW is approximately 20–25 atomic spacings depending on the temperature, so the SDW reflections appear separated by $\delta \approx 0.05$ – 0.04 from the (001) reflection at positions $(\pm\delta 0 1)$, $(0 \pm\delta 1)$ and $(0 0 1 \pm\delta)$. This group of six possible SDW reflections appears near each

of the forbidden reflections of the bcc lattice. The intensities of the SDW reflections depend on the cross sections for magnetic scattering, which are a function of the spin polarization and x-ray wavevectors.

Non-resonant magnetic scattering from Cr is well-understood in terms of the magnetic cross section [22, 25] as described in section 2.1. Because the SDW is composed primarily of itinerant magnetic spins with little orbital moment contribution, the resonant enhancement of magnetic scattering at the K -edge of Cr is weak [25, 36]. Resonant effects appear mainly as the development of a small probability of scattering while rotating the polarization [36]. Density functional theory calculations using the local density approximation show that the orbital moment in Cr is approximately a factor of ten smaller than in ferromagnetic Fe, Co or Ni and that the orbital magnetic moment arises through a spin orbit interaction with the SDW [98]. In practical terms, the overall resonant enhancement of scattering does not outweigh the increase in the absorption and fluorescence at the resonance.

The strain wave in Cr appears in reciprocal space as a satellite peak with twice the modulation wavevector of the SDW. X-ray reflections of the strain wave are found near each allowed Bragg reflection of the Cr lattice. The strain wave reflections depend only on the response of the lattice to the SDW and thus depend only the direction and magnitude of \mathbf{Q} and not on the polarization of the SDW. Most importantly, the intensity of scattering from strain waves depends on the dot product of the scattering wavevector \mathbf{q} with the lattice modulation direction \mathbf{Q} , so that even with equal domain populations the strain wave reflections at $(\pm 2\delta\ 0\ 2)$ and $(0\ \pm 2\delta\ 2)$ are orders of magnitude weaker than the reflections with \mathbf{q} parallel to \mathbf{Q} at $(0\ 0\ 2\pm 2\delta)$. The strain wave reflections are directly connected to the magnetic domains. The reflection at $(0\ 0\ 2-2\delta)$, for example, appears only for volumes of the Cr crystal where the SDW \mathbf{Q} is along the [001] direction.

The magnetic x-ray reflections near the forbidden (001) reflection can each be used to form images of the magnetic domains in Cr. The satellite reflections occur in three pairs, displaced along the H , K and L directions of reciprocal space with respect to the (001) reflection. Each pair of reflections appears in reciprocal space only if the volume of Cr illuminated by the x-ray beam contains material with \mathbf{Q} along that direction. The $(0\ 0\ 1\pm\delta)$ reflections, for example, occur only where \mathbf{Q} points along [001]. A similar rule holds for domains in which \mathbf{Q} is along [100] or [010].

The intensity of the magnetic reflections depends on the scattering geometry. Because the magnetism of Cr arises purely from electron spin angular momentum, the cross section given in equations (1) and (2) can be simplified. The intensity of the magnetic scattering from Cr is proportional to

$$[\mathbf{S}(\mathbf{Q}) \cdot (\hat{\mathbf{k}} \times \hat{\mathbf{k}}')]^2 + \left[\frac{Q^2}{2k^2} \mathbf{S}(\mathbf{Q}) \cdot \hat{\mathbf{k}} \right]^2. \quad (7)$$

When the detector integrates both polarizations of the diffracted beam, the cross section is independent of the polarization of the incident beam. Here Q and k are the magnitudes of the x-ray wavevector and the momentum transfer, respectively. The factor $Q^2/2k^2$ is equal to $2\sin^2\theta_{\text{Bragg}}$ and makes the contribution of the second term

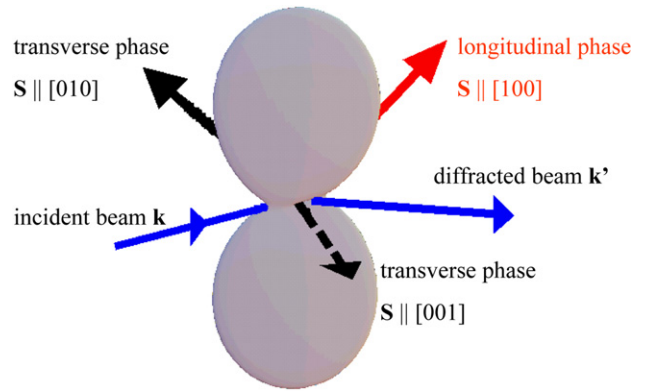


Figure 7. The non-resonant magnetic x-ray scattering cross section for Cr depends on the relative directions of the magnetic spin and the incident and diffracted beams. The three possible spin polarization directions for sample mounted as shown in figure 8 are indicated by arrows.

much smaller than the first at hard x-ray photon energies. For hard x-ray photon energies near the Cr K edge, at the $(0\ 0\ 1-\delta)$ reflection as in [25] and [99], $Q^2/2k^2$ is approximately $1/16$. To a good approximation, the resulting cross section is thus $[\mathbf{S}(\mathbf{Q}) \cdot (\hat{\mathbf{k}} \times \hat{\mathbf{k}}')]^2$, which is proportional to the magnitude of the spin pointing out of the diffraction plane defined by $\hat{\mathbf{k}}$ and $\hat{\mathbf{k}}'$. A polar plot of the non-resonant magnetic cross section in figure 7 is shown for the $(0\ 0\ 1-\delta)$ reflection but applies qualitatively to all of the magnetic reflections near (001). Because the six magnetic reflections near (001) are separated by angles of only a few degrees at photon energy 5.8 keV, this qualitative description of the spin-direction dependence of the cross section for non-resonant magnetic scattering does not depend on which \mathbf{Q} domain is used to construct the image. The only change is that the factor of 16 difference in intensity between spin polarizations is decreased to 14 because the scattering plane no longer exactly lines up with the [001] direction.

X-ray topography studies of antiferromagnetic domains in Cr have previously made use of strain wave Bragg reflections. Although the original experiments of Ando and Hosoya [100] were performed at spatial resolutions of only several hundreds of microns, topography experiments at modern light sources could in principle yield spatial resolutions $1\ \mu\text{m}$ or better. Topography studies using the strain wave reflections lacks the magnetic contrast that allows the spin polarization domains to be distinguished. Neutron topography [101–103] has been used with millimetre scale resolution in the past to image Cr domains but has fewer prospects for progressing to micron or nanometre scales.

4.1.3. Antiferromagnetic domain imaging in Cr using magnetic x-ray microdiffraction. The geometry of a microdiffraction experiment to image domains of both the SDW propagation vector \mathbf{Q} and the spin polarization \mathbf{S} is shown in figure 8. The sample, incident beam and diffracted beam are arranged to study the family of magnetic reflections near (001) for a (111)-oriented Cr single crystal. The (111) orientation does not pin the \mathbf{Q} direction along the surface normal, as occurs in crystals of other orientations, and thus allows domain populations characteristic of the bulk to be maintained in the

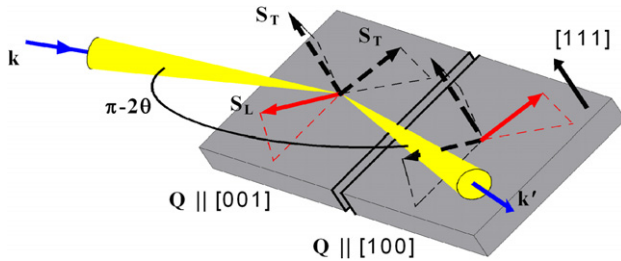


Figure 8. X-ray microdiffraction from a (111)-oriented Cr single crystal. The wavevectors of the incident and diffracted beams, \mathbf{k} and \mathbf{k}' , define the scattering plane. Domains with the antiferromagnetic ordering direction along (001) and (100) each have different directions for the spin polarizations in the longitudinal magnetic phase (solid arrows) and two possible spin polarizations in the transverse magnetic phase (dashed arrows).

near-surface region accessible to the focused x-ray beam. The incident energy of 5.8 keV was chosen to be well below the Cr K absorption threshold of 5.95 keV in order to suppress background due to sample fluorescence that would otherwise overwhelm the weak magnetic reflection.

With the scattering geometry shown in figure 8 spins polarized along the [001] direction are in the diffraction plane and have a small cross section for magnetic scattering. Spins polarized along either [100] or [010] have a significant component along $\hat{\mathbf{k}} \times \hat{\mathbf{k}}'$ and a much larger cross section for magnetic scattering. These rules-of-thumb aid in interpreting the maps of the magnetic scattering intensity as a function of position (table 1).

Scanning images of a Cr (111) crystal are shown in figure 9 for two independent scattering wavevectors [99]. Figure 9(a) is an image of the intensity of the magnetic (001- δ) reflection at a beam energy of 5.8 keV with the Cr crystal at 140 K, in the high-temperature transverse SDW phase. The image records the intensity of this reflection as a function of position. In the regions of intense scattering the magnetic Bragg condition is satisfied. These areas thus have the antiferromagnetic propagation wavevector along [001]. Adjacent areas in which the modulation vector is along [100] or [010] do not contribute to the (001- δ) magnetic reflection because the Bragg condition is not satisfied (figure 9 (c)). Magnetic scattering leads to count rates of 10–30 photons per second on the magnetic domain; maps of a large area require on the order of 1 h per scan with present x-ray sources. The same domains can also be seen in maps using the strain wave reflection at (002- 2δ) (figure 9(b)). The strain wave produces a purely charged x-ray reflection so its intensity does not depend on the magnitude of the non-resonant magnetic scattering cross section. Clearly, the regions of intense scattering from the strain wave agree with the regions of intense magnetic scattering.

Since Cr is in the transverse SDW phase at $T = 140$ K, both spin polarizations within the domains with the modulation vector along [001] satisfy the rule-of-thumb selection rule described above. The magnetic sensitivity of the magnetic reflection can be shown by cooling through the Cr spin-flip transition at $T_{\text{SF}} = 123$ K. Comparing the SDW and strain wave reflections of a region with a single domain acquired at temperatures of 130 and 110 K, just above and below T_{SF} , shows that although the domain of antiferromagnetic

propagation vector in the [001] direction persists unchanged through the spin-flip transition the magnetic reflection disappears because the cross section is negligible for spins polarized along [001] [103] (figure 10).

The reflections at $(\pm\delta\ 0\ 1)$ and $(0\ \pm\delta\ 1)$ belong to regions in which \mathbf{Q} points along [100] or [010]. The rule-of-thumb magnetic scattering selection rules are the same in these domains as in domains with \mathbf{Q} along [001], but their effect on the visibility of low- and high-temperature magnetic phases is different. For the [001] modulation direction domains of the transverse phase, the magnetic cross section shown in figure 7 allows both spin polarizations to produce intense Bragg reflections. In [100] and [010] modulation direction domains one of the spin polarizations lies approximately within the scattering plane. Only the spin polarization with a large component out of the scattering plane produces a strong diffracted beam.

The images shown in figure 11 take advantage of these selection rules to map both the spin polarization and \mathbf{Q} . In the low temperature longitudinal phase (figure 11(a)) the reflections from regions in which \mathbf{Q} is along [100] or [010] show strong domains that fill a large portion of the total area. The dark area belongs to a domain with \mathbf{Q} oriented along [001] that cannot be seen even when the Bragg condition is satisfied because the cross section for magnetic scattering from the longitudinal phase of domains with \mathbf{Q} along [001] is negligible. At 140 K magnetic scattering from all three domains of the ordering wavevector is visible (figure 11(b)). The remaining dark areas correspond to regions of the Cr crystal where the magnetic cross section is small in the transverse phase. Thus, the dark areas within the [100] and [010] ordering direction domains are regions where the spin is polarized along [001].

This sensitivity to the local spin polarization allows us to understand and manipulate magnetic domains on a new set of length scales. Evidence suggests that the presence of magnetic domains could be important in transport and magnetotransport effects. Manipulating these domain walls for antiferromagnetic technology will be possible only with a structurally specific diagnostic tool.

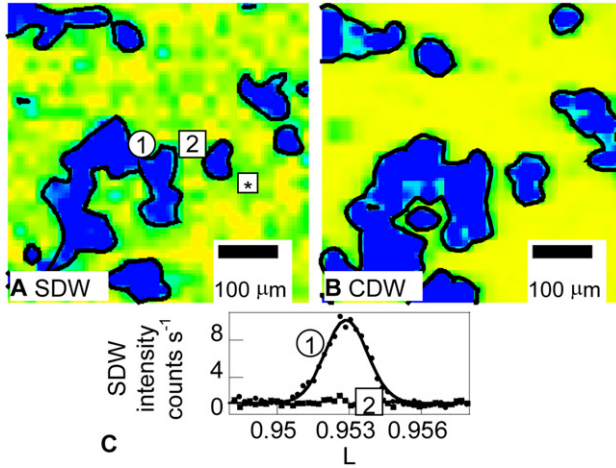
4.2. Diffraction probes of magnetic domains in ferrimagnetic HoFe₂

In comparison with antiferromagnetic materials, for which there are relatively few techniques that can be used to study individual domains, ferromagnetic and ferrimagnetic materials are much more easily probed. The link between magnetism and structure in this broad class of materials can be probed quantitatively only by techniques that combine structural and magnetic sensitivity. In this section, a demonstration of the potential to image domains in HoFe₂, a ferrimagnet, shows how future experiments can potentially lead to a better understanding of the link between structural and magnetic phenomena.

HoFe₂ has a high Curie temperature, low coercive magnetic field and large magnetic moment. HoFe₂ is a cubic Laves phase metallic compound with the MgCu₂ structure [104] with Ho ions on a diamond sublattice (figure 12). Below $T_C = 612$ K, Ho is ferrimagnetic with a large saturation moment. The net magnetic moment can be oriented in

Table 1. A summary of the magnetic cross section selection rules for the Cr in the x-ray scattering geometry shown in figure 8.

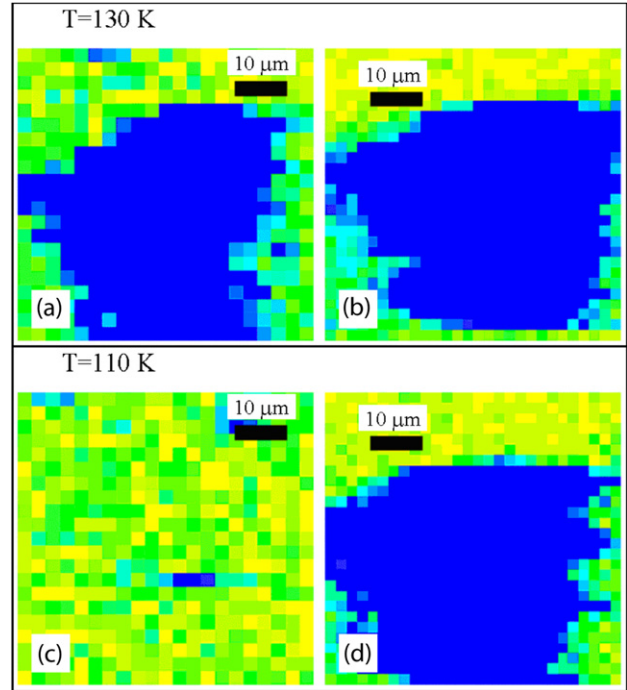
	<i>H</i> Domains	<i>K</i> Domains	<i>L</i> Domains
Reflections	$(\pm\delta 0 1)$	$(0 \pm\delta 1)$	$(00 1 \pm\delta)$
Transverse phase ($T > 123$ K)	Visible only in areas with <i>S</i> along <i>K</i> direction	Visible only in areas with <i>S</i> along <i>H</i> direction	Visible for both <i>S</i> polarizations
Longitudinal phase ($T > 123$ K)	Visible	Visible	Not visible

**Figure 9.** Images of a $500\ \mu\text{m} \times 500\ \mu\text{m}$ region of a Cr single crystal using (a) the $(00 1 -\delta)$ SDW reflection and (b) the $(00 2 -2\delta)$ strain wave reflection. (c) Reciprocal space scans along *L* at the points (1) and (2) demonstrate that the areas of intense scattering arise from x-ray reflections with a well-defined wavevector.

any of the $\langle 001 \rangle$ directions of the host lattice. There are six magnetization directions and thus six possible magnetic domains in the ferrimagnetic phase. The coercive magnetic field is low and thus the magnetization direction can be switched by a modest applied field. Pollmann *et al* combined zone plate x-ray focusing optics with a diamond phase plate to produce a circularly polarized $4.0 \times 2.3\ \mu\text{m}^2$ probe beam and made maps of the local magnetization within a HoFe₂ crystal [105].

The distribution of the magnetism of HoFe₂ between Ho and Fe, and the relative contribution of spin and orbital moments to the total magnetization have been carefully determined with non-resonant magnetic x-ray diffraction [106, 107], magnetic Compton scattering and magnetic neutron scattering [108]. In the ordered ferrimagnetic phase, the Fe and Ho ions have magnetizations of opposite signs. Ho has the dominant contribution at 300 K, amounting to $+6.3\ \mu_B$ per Ho ion. The magnetization of the Fe ions is in the opposite direction with a moment of $-1.85\ \mu_B$ at $T = 300$ K [24]. The total moment, including a diffuse contribution that is not localized at either Fe or Ho sites, is $\mu_{\text{sat}} = 2.73\ \mu_B$ per unit cell [107].

The most important source of magnetic scattering from HoFe₂ arises from an electric dipole x-ray resonant exchange scattering process at photon energies near the Ho L_{III} absorption edge [16] at 8.07 keV. The magnetic scattering amplitude f_M depends on the incident and outgoing polarizations, $\hat{\epsilon}$ and $\hat{\epsilon}'$, respectively, and on the local magnetization direction on the Ho ion, \mathbf{M} (figure 13). The overall magnitude of f_M is determined by the degree to which

**Figure 10.** Upper panel: images in the transverse SDW phase of the (a) $(00 1 -\delta)$ magnetic reflection and (b) $(00 2 -2\delta)$ strain wave reflection. The colour scale ranges from bright (lowest intensity) to dark (highest intensity) and was chosen to emphasize the domain contrast. Lower panel: images with the sample at 110 K in the longitudinal SDW phase. The intensity of the magnetic reflection (c) has diminished due to the rotation of the spin polarization upon cooling through the spin-flip transition. The strain wave reflection (d) is unchanged, after [103].

the filled and empty states of the Ho L_{III} resonance are spin-polarized. The magnetization of Ho has a strong resonant enhancement factor for photon energies near the Ho L_{III} edge. At this absorption edge, the dipole term $F^{(1)}$ dominates in equation (6) and the overall magnetic scattering amplitude is

$$f_M = -iF^{(1)}(\hat{\epsilon}'^* \times \hat{\epsilon}) \cdot \mathbf{M}. \quad (8)$$

The magnetism \mathbf{M} of the Ho ion can be probed by measuring the normalized difference in intensity of the (004) reflection with incident beams of two different helicities. This asymmetry in the intensity of the scattered radiation with respect to the incident polarization is analogous to the flipping ratio of magnetic neutron scattering. The dominant magnetic scattering cross section arises from an interference between Thomson scattering (equation (2)) and magnetic scattering (equation (7)). The dependence of the interference on the magnetization of the sample and the Bragg angle θ_B can be found by combining the polarization dependence of the

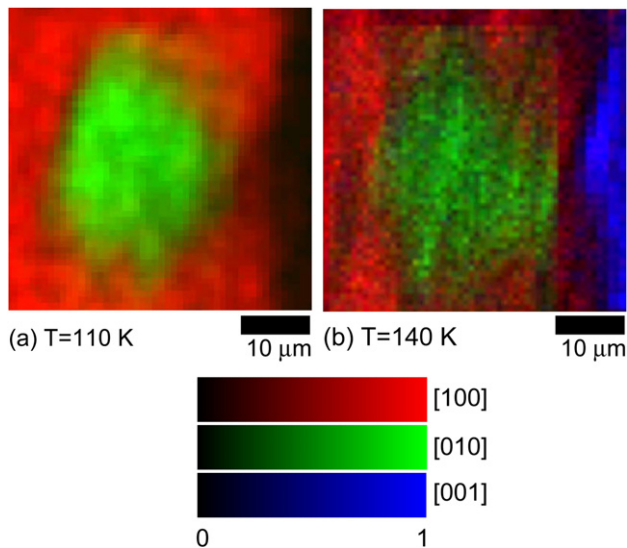


Figure 11. Magnetic microdiffraction images of a Cr (111) single crystal at (a) 140 K and (b) 110 K. The intensities of x-ray reflections near (001) belonging to domains in which \mathbf{Q} is oriented along [100], [010], and [001] are shown in individual intensity scales.

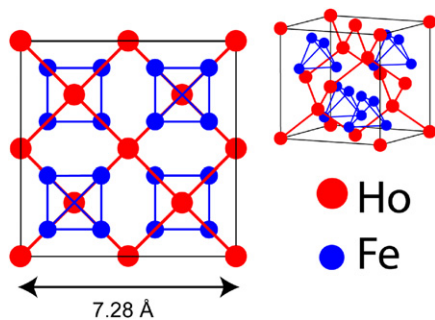


Figure 12. Crystal structure of HoFe_2 .

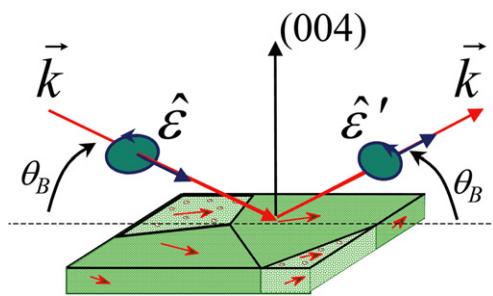


Figure 13. Polarization and wavevectors of incident and diffracted beams in an x-ray magnetic microdiffraction study of HoFe_2 .

interference reflection derived by Blume *et al* [30] with the dependence of the resonant scattering cross section on the magnetization of HoFe_2 [43, 45].

Pollman *et al* used a circularly polarized beam for which the degree of circular polarization expressed as the circular component of the Poincaré–Stokes vector was $P_c \sim 0.99$ [105]. In this imaging experiment, the helicity of the focused x-ray beam was switched rapidly between left- and right-circular polarizations to isolate the magnetic contribution to the HoFe_2 (004) Bragg reflection. An asymmetry ratio R can be used to interpret the helicity dependence of the results. The asymmetry ratio $R = (I_{\text{RCP}} - I_{\text{LCP}})/(I_{\text{RCP}} + I_{\text{LCP}})$ depends

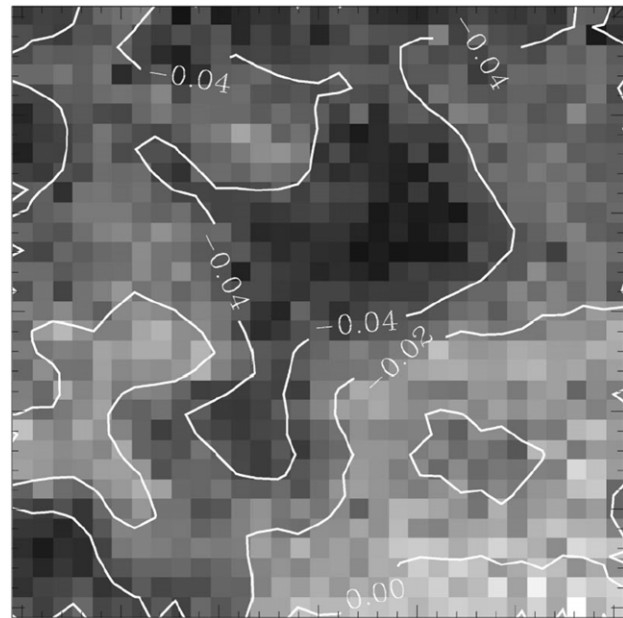


Figure 14. Image of the magnetic asymmetry ratio of intensities of the diffracted beams produced at the HoFe_2 (004) reflection using incident radiation of opposite helicities with $H = 0$, after [105].

on I_{RCP} and I_{LCP} , the intensities of the diffracted beam measured with right- and left-circularly polarized and incident radiation, respectively. In terms of the Bragg angle θ_B and the components of magnetization in a coordinate system of the surface, the asymmetry ratio is

$$R \approx F(\omega_0)(M_x \cos \theta + M_z \sin \theta)(1 + \cos 2\theta). \quad (9)$$

Here M_z points along the surface normal and M_x points in the direction of the projection of the incident beam wavevector along the sample surface. A third component of the magnetization, M_y , points along the surface of the sample in the direction perpendicular to both the incident and diffracted beams.

Local values of R for the (004) reflection of HoFe_2 ranged from -0.07 to 0.03 [105]. Because the magnitude and sign of R depend on the local direction of the magnetization, maps of R , as in figure 14, can be used to distinguish domains of magnetization direction. Equation (9) can be used to interpret the relative intensities of regions of figure 14. Areas with high positive or negative values of the asymmetry ratio had large values of M_x or M_z . Where the magnitude of the asymmetry ratio was near zero the magnetization was polarized along the y direction.

The quantitative interaction between x-ray photons and the magnetization makes several control experiments possible. The response of the magnetization to an applied magnetic field larger than the coercive field was quantitatively consistent with the predicted asymmetry ratio. When a $H = 3$ kG magnetic field was applied to the sample the magnetic asymmetry ratio saturated at a single uniform value consistent with the description above. In addition, the magnetic signal did not depend on the intensity of the Bragg reflection of HoFe_2 , which can be found by plotting $I_{\text{RCP}} + I_{\text{LCP}}$ as a function of position.

The images of magnetic domains in HoFe_2 use the interference between a Bragg reflection of the crystalline

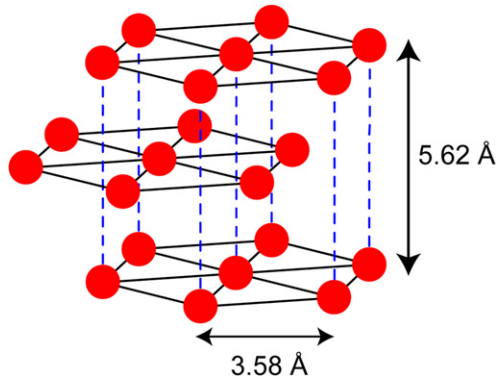


Figure 15. The crystal lattice of elemental Ho. The low temperature magnetic structures observed in Ho crystals appear in figure 5(e).

lattice and the magnetic scattering amplitude to probe the local magnetization of a crystal. Because the probe uses Bragg diffraction to measure the magnetization, it probes only the ion resonant with the incident x-ray energy and only the structure with the appropriate Bragg reflection. This degree of specificity will be crucial in probing magnetic ions in heterostructures in which a specific layer is distinguished from other layers by only a small structural difference.

4.3. Domains of spiral antiferromagnetism in elemental Ho

The complexity of magnetic structures allows diffraction probes to couple to subtle magnetic ordering phenomena that cannot be visualized with other techniques. Lang *et al* have used magnetic diffraction techniques to study the spiral antiferromagnetic domains in elemental holmium [109]. Between 19 and 133 K, the magnetic structure is an antiferromagnetic spiral in which spins are ferromagnetically aligned in each close-packed plane of the hexagonal close-packed lattice (figure 15) and each subsequent plane is offset at an angle corresponding to a spiral wavevector τ (figure 5(e)). The direction of the spiral is aligned with the [001] direction of the Ho crystal lattice so that at each volume of the crystal there are two possible domain states distinguished only by the sign of τ . The handedness of the spiral structure is determined by the sign of τ . The spirals have a period corresponding to several lattice spacings. In terms of the c^* , the reciprocal lattice vector associated with the [001] direction in Ho, the magnitude of τ ranges from 0.16 c^* at high temperature to 0.3 c^* at low temperatures.

Ho has been widely used as the test case for both resonant and non-resonant magnetic x-ray scattering techniques. The spiral magnetic structure of holmium leads to relatively strong magnetic x-ray reflections that are well-isolated in reciprocal space from the charged reflections. These reflections can be observed in both resonant and non-resonant x-ray scattering experiments [23, 33, 110]. The resonant scattering from the L_{III} edge in particular has served to demonstrate the atomic origin of magnetic reflections and to verify the usefulness of the quantum mechanical description of resonant scattering. Scattering of circularly polarized incident radiation can be linked to specific terms of the scattering factor and can be used to elucidate the helicity of the magnetic spiral structure. As with HoFe_2 , the strongest resonant contribution to first-order

magnetic reflections arises from electric dipole transitions at the Ho L_{III} absorption edge.

The cross section given by Hill and McMorow for helical structures can be adapted to circularly polarized incident beams [20]. When this is done, a series of superlattice reflections at wavevectors τ , 2τ , 3τ and 4τ relative to the structural Bragg reflection is found. Only the expression in equation (10) leads to an x-ray reflection at the first order (i.e. separated from a structural reciprocal lattice point G by τ) with an intensity proportional to the sign of the circular polarization. This term is proportional to

$$P_c [\delta(Q + \tau - G) - \delta(Q + \tau + G)]. \quad (10)$$

The important point in interpreting the resonant magnetic scattering cross section is that it is proportional to P_c , the sign of the helicity of the incident beam. The asymmetry ratio of a Bragg reflection from the magnetic spiral is proportional to the term in equation (10).

Spiral magnetic structures of both chiralities lead to x-ray reflections at the same point in reciprocal space. Each reflection of the spiral structure carries with it a particular handedness. The reflection at $(0\ 0\ 2+\tau)$, for example, is actually at $G + \tau$ when it is generated by a spiral with its helicity with τ along the positive z direction and at $G - \tau$ for the opposite helicity. The sign of equation (9) thus depends on the helicity of the structure being probed. Changing either the helicity or the handedness of the circular polarization switches the sign of this term. The sign of the change in intensity of the magnetic reflection of a particular volume of material when the incident circular polarization is switched thus reveals the helicity of the structure being probed. With circularly polarized x-rays, the sign of the change in intensity accompanying a change in x-ray helicity thus depends on the helicity of the spiral.

The magnetic reflections separated by τ from allowed Bragg reflections of the Ho atomic lattice can thus be used to make spatially resolved maps of helicity domains if the incident beam is small enough to illuminate only a single domain. The resonant properties and relative populations of domains have traditionally been probed only in area-integrated measurements with unfocused x-ray beams [111] and in imaging experiments using neutron topography at the millimetre scale.

Lang *et al* have used this scattering effect to image helical antiferromagnetic domains in a single crystal of holmium [109]. They combined spatially resolved x-ray diffraction using a $25\ \mu\text{m}$ beam produced with an aperture and magnetic scattering to make image domains of the helical antiferromagnetic domains within a Ho single crystal. The images of the value of the magnetic asymmetry ratio shown in figure 16 were made with two distinct reflections, located at opposite displacements in reciprocal space relative to the (002) structural Bragg peak. Both images show the same domain pattern, but with opposite contrast, which is consistent with the cross section in equation (9).

The area integral of each image of the images of helical domains in Ho (figure 16) is close to zero, as would be expected when the populations of domains of the two helicities are approximately equal [109]. In addition, the maximum local value of the asymmetry ratio is greater than the average

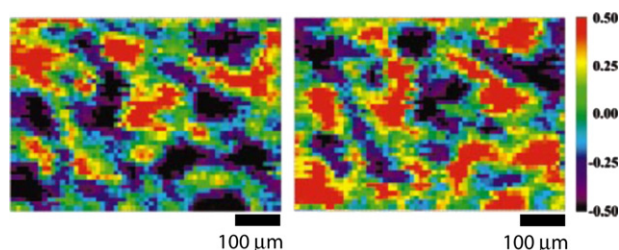


Figure 16. Images of domains of antiferromagnetic helicity in elemental Ho using reflections at $(0\ 0\ 4 + \tau)$ (left image) and $(0\ 0\ 4 - \tau)$ (right image), after [109].

flipping ratio observed with a larger beam. The larger, millimetre-scale x-ray beams probe the average response of the crystal, which involves an unknown population of domains and may be difficult to interpret given this ambiguity. X-ray microdiffraction experiments provide the possibility of studying magnetic scattering in a way that is free of these complications. The ability to probe these domain structures is the first step in connecting them to a variety of physical phenomena.

Kim *et al* have [112] similarly imaged antiferromagnetic domains in GdNiGe_2 using resonant scattering at the L_{II} edge of Gd. GdNiGe_2 has two low temperature phases that had not been understood structurally in large-scale measurements but which can be distinguished using imaging techniques. In this case, the quantitative cross section and ability to form images under well-defined experimental conditions allow the origin of contrast in images to be related to the magnetic structure unambiguously. In GdNiGe_2 the magnetic microdiffraction images allowed a phase transition that had been observed in specific heat measurements to be attributed to a transition from a high-temperature collinear antiferromagnetic phase stable between 27.5 and 16 K to a low-temperature antiferromagnetic spiral [112].

5. Applications

A common aspect of many important problems in the physics and applications of magnetic materials is that the interaction between magnetization, structure, chemical state and external fields at small scales is inherently important. The physics of complex magnetic order in these problems at the scales of times for acoustic propagation over several microns, on the scale of 1–10 ns, is unexplored.

5.1. Magnetic and multiferroic complex oxides

5.1.1. Multiferroics. Multiferroics are a broad class of materials that exhibit both ferroelectricity and magnetism. The possibility of manipulating electronic and magnetic polarizations simultaneously has driven an intense recent interest in multiferroic complex oxides [110]. These materials have built-in ferroelectric polarizations which can be as large as common ferroelectrics such as $\text{Pb}(\text{Zr,Ti})\text{O}_3$ (PZT) in addition to appreciable magnetic order. The most interesting materials have both these polarizations at room temperature and, despite some structural complexity, can be grown as stable thin films. The parametrization of the response of multiferroics to external fields involves a large number of potentially

important constitutive relations. For example, in addition to the traditional couplings between stress and strain, there is the new potential to couple strain to magnetization, ferroelectric polarization or even to the overall stability of a structural phase. X-ray studies of the magnetic oxide $(\text{La,Sr})\text{MnO}_3$ have shown that small changes in the biaxial strain arising from epitaxial growth can result in large changes in the magnetic critical temperature [113]. Multiferroics extend the potential range of couplings to another degree of complexity because strain, magnetization and polarization are interrelated.

The magnetism of multiferroic materials often stems from ions with high magnetic moments. A recently discovered multiferroic HoMnO_3 has the expected large moment on the Ho ion at low temperatures, exhibiting antiferromagnetic ordering of moments associated with Mn ions below $T_N = 75$ K, and ferroelectricity below $T_C \approx 800$ K [114]. An electric field of 10^5 V cm^{-1} promotes ferromagnetic ordering of Ho ions at a much higher temperature than that observed at $E = 0$. This effect is analogous to shifts in the Curie temperature of the ferroelectric-paraelectric phase transition in ferroelectric BaTiO_3 and in the magnetic Curie temperature of $(\text{La,Sr})\text{MnO}_3$ by a static biaxial strain [92]. Similarly, a magnetic field can be used to control the ferroelectric polarization in TbMnO_3 . The ferroelectric Curie temperature of TbMnO_3 was lowered by more than 20 K in a $H = 9$ T magnetic field [115].

Bismuth ferrite is a compound that has been synthesized since the early 1960s in its bulk rhombohedral form [116, 117]. In this form, BiFeO_3 is antiferromagnetic with a Néel temperature far above room temperature. Thin films of BiFeO_3 on substrates with significant lattice mismatches have a modified crystal structure that is stabilized by the strain resulting from epitaxial growth. A series of static x-ray diffraction experiments has found that the stable thin film structure is a monoclinic lattice produced by a small distortion of a tetragonal structure [118]. These thin films also have much higher remnant polarization than bulk materials, in part because their greater structural perfection is more conducive to small leakage currents in the presence of large electrical fields but also because the stabilized structure is thought to lead to higher ferroelectric polarization [119]. Thin films of BiFeO_3 can easily be integrated with layers of conducting oxides with similar crystal structure, such as SrRuO_3 , allowing thin films of excellent crystalline quality to be integrated into capacitor structures. While the ferroelectricity of BiFeO_3 thin films has now been confirmed in several studies [120], the structure and magnetism are still debated. Eerenstein *et al* found that films structurally similar to those of [119] have far smaller magnetization than expected ($0.04 \mu_B$ per Fe versus $1 \mu_B$ per Fe) and suggested that the magnetism of the films of Wang *et al* arises from impurity phases rather than from BiFeO_3 [121]. X-ray microdiffraction has the potential to shed light on these types of controversies by probing the magnetism of structurally using diffraction and by including the dynamical response of the structure to electric fields in the understanding of the magnetism.

The interaction of magnetic and ferroelectric moments remains important question. X-ray microdiffraction techniques have the potential to probe strain and polarization simultaneously in piezoelectric structures. The dynamic relationship between these quantities and magnetization in

multiferroic materials will be an important application of magnetic x-ray microdiffraction.

5.1.2. Inherent inhomogeneity and phase competition in magnetic manganites. The links between structure, chemistry and magnetic phenomena are equally important when the magnetic and electronic phases are differentiated by chemical doping. Manganese oxides have electronic and magnetic phases that follow a phase diagram controlled by the electron phonon coupling, which is in turn controlled by doping [122]. (La,Sr)MnO₃ is a prototypical manganite in which doping with Sr is used to tune between charge-ordered insulating, ferromagnetic insulating and ferromagnetic metal states starting from the LaMnO₃ parent compound. As briefly discussed in the previous section, a small strain can also be sufficient to cause drastic changes in the doping temperature phase diagram. Soh *et al* found that a relaxation of the biaxial strain induced in a (La,Sr)MnO₃ thin film during epitaxial growth on SrTiO₃ could shift magnetic phase boundaries by tens of degrees [92].

The potential for long-range strain, magnetic- or electric-field-mediated interactions in a wider class of materials has led to a second distinct theme in multiferroic materials: digital structures [123]. These can be laminated composites, which have existed for decades, but also include a recent class of self-organized structures at the scale of tens of nanometres [124, 125].

In addition to the large sensitivity to applied fields, there is the potential in these materials for long-range order based on the arrangement of Mn³⁺ and Mn⁴⁺ ions and orbital directions in addition to ferromagnetism [113, 126]. An important question remains whether the region near the phase boundary between doping regimes leads to an *inherent* inhomogeneity analogous to the formation of a new phase. The length scale, dynamics and stabilities of the proposed inhomogeneity varies [122]. X-ray techniques have the potential to probe these questions in extreme environments, including low temperatures and high mechanical deformations. X-ray dichroism effects will allow the magnetism of each magnetic ion to be probed independently, for example, using the Ho *L*_{III} and Mn *K* resonances in HoMnO₃.

5.2. Nanomagnetism: interface and domain wall structures, interactions and electronic properties

The potential to manipulate magnetism at small length and timescales has led to a vastly improved understanding of the science and technological applications of magnetic structures. Much of this understanding involves the creation and manipulation of magnetic interfaces, which can have profound effects on magnetic transport and dynamics. Magnetic nanostructures have tiny total magnetic moments but fascinating static and dynamic magnetic properties.

Magnetic domain walls and interfaces in metal heterostructures [127, 128] have a large effect on electronic transport due to the mismatch in localized states at the domain wall. Devices such as vertical and lateral spin valves have a large magnetoresistance that arises from an analogous manipulation of the relative magnetic states of the components of a nanostructure. These structures are

the basis for data storage devices including giant magneto-resistance read heads. The magnetic structure of thin film devices is also affected by interface effects including exchange bias and the influence of spin polarized currents on local magnetic moments. Neutron scattering and Mossbauer studies can provide some indication of the role of domains in these multilayers but antiferromagnetic domains and the state of films buried under chemically similar layers is less well known [129].

The effects of magnetic structure on electronic transport have typically been studied in transport experiments coupled with magnetic microscopy techniques using devices with just a few domains [130] or with long range order in the domain structure [131]. Magnetic x-ray microdiffraction has the potential to extend the understanding of magnetic interfaces and dynamics to more intricate magnetic structures and interfaces, for example, between two antiferromagnets. These studies allow the potential to engineer with antiferromagnets and other complex magnetic structures at the same degree of precision as conventional magnetic metals. Magnetic x-ray microdiffraction adds high speed, small spot sizes, the potential to penetrate intricate device structures and elemental specificity to existing techniques and thus also has the potential to complement existing approaches to magnetic microscopy, even in understanding ferromagnetic nanostructures and devices. The coherent transport of spins requires a detailed understanding of the underlying magnetic structure. It is unlikely that x-ray probes will be capable of observing the polarized spin current directly. The effects of these currents in layered [132–134] and lateral structures can be visualized directly using x-ray techniques.

Nanoparticles can have magnetic properties unattainable in the bulk, including high ferromagnetic transition temperatures and the stabilization of otherwise unstable phases. A fundamental example is the exchange bias known for many years to result from the presence of Co oxide on the surface of Co metals nanoparticles. The connections between these altered magnetic properties and the structural or chemical phenomena at nanoparticle interfaces can be probed together in the single- or few-nanoparticle limit using x-ray microdiffraction.

5.3. Magnetic dynamics

The dynamics of magnetic materials include both local phenomena such as coherent spin precession and relaxation and long-range phenomena including transport of spins and the propagation of domain walls. The time scales of these phenomena are coupled not only to the fundamental magnetic interaction between nearby moments but also to the thicknesses of films and lateral extent of device structures.

Domain wall propagation, for example, can occur at speeds comparable to the propagation of sound [135]. Imaging domain wall propagation at the relevant lengths for devices is fundamentally important. In ferromagnetic materials and near surfaces this can be accomplished with magneto-optics and soft x-ray dichroism techniques [77, 136]. Magnetic x-ray microdiffraction can extend the range of materials for which it is possible to observe domain propagation by examining the magnetic order that is not visible to other probes. Similarly,

the precession of the overall magnetization of nanostructures depends on device-scale lengths [87, 137]. A second frontier in understanding magnetic dynamics is in the coherent transport of magnetic information in spin waves [138] or in spin-polarized currents [139]. The timescales for these phenomena are set at the microscopic scale by fundamental spin-relaxation times or spin-wave frequencies. Time resolutions of tens of picoseconds are necessary to understand these effects in nanostructures. With better time resolution, it will be possible to probe the magnetic phenomena that lead to the development of spin coherence over long scales and the fundamental response of moments to fields. At present these studies can only be done after picosecond-scale pulses [140]. Short-pulse x-ray sources have the potential to extend the structural magnetic techniques we have reviewed here to the timescale relevant for these phenomena.

6. Conclusion

Time-resolved techniques have the potential to move magnetic structural and microscopy techniques away from imaging time-averaged or time-invariant structures to look at the real-time evolution of magnetic structures. Magnetic dynamics are already probed by inelastic scattering techniques, but these techniques lack spatial resolution and probe excitations only at energies equivalent to extremely short times. X-ray microdiffraction techniques have the potential to study long-range dynamical excitations with spatial and structural specificity.

Just as exciting is the potential to combine coherent x-ray scattering with magnetic microdiffraction either for studies of dynamics using photon correlation spectroscopy or to produce three-dimensional reconstructions of magnetic structures using coherent reconstruction techniques. X-ray-focusing optics preserve the coherence of the focused beam. Structural Bragg reflections have already been used in inversion experiments to produce three-dimensional maps with tens of nanometre-scale spatial resolution [141]. The extension of these techniques to magnetic reflections requires an increase commensurate with the weakness of magnetic reflections in either the time required to accumulate the diffracted signal or in source intensity which may become possible with the next generation of optics and x-ray sources.

© US Government

References

- [1] Moser A, Takano K, Margulies D T, Albrecht M, Sonobe Y, Ikeda Y, Sun S and Fullerton E E 2002 *J. Phys. D: Appl. Phys.* **35**R157
- [2] Prandl W 1978 *Neutron Diffraction* ed H Dachs (Berlin: Springer)
- [3] Ice G E, Hubbard C R, Larson B C, Pang J W L, Budai J D, Spooner S and Vogel S C 2005 *Nucl. Instrum. Methods A* **539** 312
- [4] Eskildsen M R, Gammel P L, Isaacs E D, Detlefs C, Mortensen K and Bishop D J 1998 *Nature* **391** 563
- [5] Freeman M R and Choi B C 2001 *Science* **294** 1484
- [6] DeCamp M F *et al* 2001 *Nature* **413** 825
- [7] Reis D A *et al* 2001 *Phys. Rev. Lett.* **86** 3072
- [8] Lovesey S W and Collins S P 1996 *X-Ray Scattering and Absorption by Magnetic Materials* (Oxford: Oxford University Press)
- [9] Als-Nielsen J and McMorrow D 2001 *Elements of Modern X-ray Physics* (New York: Wiley)
- [10] Ebert H 1996 *Rep. Prog. Phys.* **59** 1665
- [11] Stirling W G and Cooper M J 1999 *J. Magn. Magn. Mater.* **200** 755
- [12] Klein O and Nishina T 1929 *Z. Phys.* **52** 853
- [13] De Bergevin F and Brunel M 1972 *Phys. Lett. A* **39** 141
- [14] Platzman P M and Tzoar N 1970 *Phys. Rev. B* **2** 3556
- [15] Blume M 1985 *J. Appl. Phys.* **57** 3615
- [16] Blume M and Gibbs D 1988 *Phys. Rev. B* **37** 1779
- [17] Debergevin F and Brunel M 1981 *Acta Crystallogr. A* **37** 314
- [18] Durbin S M 1998 *Phys. Rev. B* **57** 7595
- [19] Warren B E 1969 *X-ray Diffraction* (Reading, MA: Addison-Wesley)
- [20] Hill J P and McMorrow D F 1996 *Acta Crystallogr. A* **52** 236
- [21] Strempler J, Bruckel T, Hupfeld D, Schneider J R, Liss K D and Tschentscher T 1997 *Europhys. Lett.* **40** 569
- [22] Strempler J, Bruckel T, Caliebe W, Vernes A, Ebert H, Prandl W and Schneider J R 2000 *Eur. Phys. J. B* **14** 63
- [23] Gibbs D, Grubel G, Harshman D R, Isaacs E D, McWhan D B, Mills D and Vettier C 1991 *Phys. Rev. B* **43** 5663
- [24] Collins S P, Laundy D and Guo G Y 1993 *J. Phys.: Condens. Matter* **5** L637
- [25] Hill J P, Helgesen G and Gibbs D 1995 *Phys. Rev. B* **51** 10336
- [26] Laundy D, Collins S P and Rollason A J 1991 *J. Phys.: Condens. Matter* **3** 369
- [27] Collins S P, Laundy D and Rollason A J 1992 *Phil. Mag. B-Phys. Condens. Matter Stat. Mech. Electron. Opt. Magn. Prop.* **65** 37
- [28] Igarashi J and Hirai K 1994 *Phys. Rev. B* **50** 17820
- [29] Stahler S, Schutz G and Ebert H 1993 *Phys. Rev. B* **47** 818
- [30] Hannon J P, Trammell G T, Blume M and Gibbs D 1988 *Phys. Rev. Lett.* **61** 1245
- [31] Lang J C, Srajer G, Detlefs C, Goldman A I, Konig H, Wang X D, Harmon B N and McCallum R W 1995 *Phys. Rev. Lett.* **74** 4935
- [32] Schutz G, Wagner W, Wilhelm W, Kienle P, Zeller R, Frahm R and Materlik G 1987 *Phys. Rev. Lett.* **58** 737
- [33] Gibbs D, Moncton D E, Damico K L, Bohr J and Grier B H 1985 *Phys. Rev. Lett.* **55** 234
- [34] Isaacs E D, McWhan D B, Peters C, Ice G E, Siddons D P, Hastings J B, Vettier C and Vogt O 1989 *Phys. Rev. Lett.* **62** 1671
- [35] Namikawa K, Ando M, Nakajima T and Kawata H 1985 *J. Phys. Soc. Japan* **54** 4099
- [36] Mannix D, de Camargo P C, Giles C, de Oliveira A J A, Yokaichiya F and Vettier C 2001 *Eur. Phys. J. B* **20** 19
- [37] Neubeck W, Vettier C, Lee K B and de Bergevin F 1999 *Phys. Rev. B* **60** R9912
- [38] Stunault A, de Bergevin F, Wermeille D, Vettier C, Bruckel T, Bernhoeft N, McIntyre G J and Henry J Y 1999 *Phys. Rev. B* **60** 10170
- [39] Neubeck W, Vettier C, Fernandez V, de Bergevin F and Giles C 1999 *J. Appl. Phys.* **85** 4847
- [40] Hill J P, Kao C C and McMorrow D F 1997 *Phys. Rev. B* **55** R8662
- [41] Lagomarsino S, Cedola A, Cloetens P, Di Fonzo S, Jark W, Soullie G and Riekel C 1997 *Appl. Phys. Lett.* **71** 2557
- [42] Golovchenko J A, Kincaid B M, Levesque R A, Meixner A E and Kaplan D R 1986 *Phys. Rev. Lett.* **57** 202
- [43] Mills D M 1987 *Phys. Rev. B* **36** 6178
- [44] Hirano K, Izumi K, Ishikawa T, Annaka S and Kikuta S 1991 *Japan. J. Appl. Phys.* **30** L407
- [45] Hirano K, Maruyama H 1997 *Japan. J. Appl. Phys.* **36** L1272
- [46] Kirz J 1974 *J. Opt. Soc. Am.* **64** 301
- [47] Lai B *et al* 1992 *Appl. Phys. Lett.* **61** 1877
- [48] Yun W 2006 private communication
- [49] Kirkpatrick P and Baez A V 1948 *J. Opt. Soc. Am.* **38** 766

- [50] Evans-Lutterodt K *et al* 2003 *Opt. Express* **11** 919
- [51] Nohammer B, Hoszowska J, Freund A K and David C 2003 *J. Synchrotron Radiat.* **10** 168
- [52] Lengeler B, Schroer C G, Kuhlmann M, Benner B, Günzler T F, Kurapova O, Zontone F, Snigira A and Snigireva I 2005 *J. Phys. D: Appl. Phys.* **38** A218
- [53] David C, Kaulich B, Barrett R, Salome M and Susini J 2000 *Appl. Phys. Lett.* **77** 3851
- [54] David C and Souvorov A 1999 *Rev. Sci. Instrum.* **70** 4168
- [55] Kang H C, Stephenson G B, Liu C, Conley R, Macrander A T, Maser J, Bajt S and Chapman H N 2005 *Appl. Phys. Lett.* **86**
- [56] Suzuki Y, Takeuchi A, Takano H and Takenaka H 2005 *Japan. J. Appl. Phys.* **44** 1994
- [57] Takano H, Suzuki Y and Takeuchi A 2003 *Japan. J. Appl. Phys.* **42** L132
- [58] Hignette O, Cloetens P, Rostaing G, Bernard P and Morawe C 2005 *Rev. Sci. Instrum.* **76** 063709
- [59] Matsuyama S *et al* 2005 *Rev. Sci. Instrum.* **76** 083114
- [60] Schroer C G *et al* 2005 *Appl. Phys. Lett.* **87** 123103
- [61] Mimura H *et al* 2005 *Japan. J. Appl. Phys.* **44** L539
- [62] Yumoto H *et al* 2005 *Rev. Sci. Instrum.* **76** 063708
- [63] Schroer C G and Lengeler B 2005 *Phys. Rev. Lett.* **94** 054802
- [64] Suzuki Y 2004 *Japan. J. Appl. Phys.* **43** 7311
- [65] Schroer C G *et al* 2003 *Appl. Phys. Lett.* **82** 1485
- [66] Kang H C, Maser J, Stephenson G B, Liu C, Conley R, Macrander A T and Vogt S 2006 *Phys. Rev. Lett.* **96** 127401
- [67] Attwood D T 2000 *Soft X-rays and Extreme Ultraviolet Radiation: Principles and Applications* (Cambridge: Cambridge University Press)
- [68] Chao W, Harteneck B D, Liddle J A, Anderson E H and Attwood D T 2005 *Nature* **435** 1210
- [69] Di Fabrizio E, Romanato F, Gentili M, Cabrini S, Kaulich B, Susini J and Barrett R 1999 *Nature* **401** 895
- [70] Yun W, Lai B, Krasnoperova A A, Fabrizio E D, Cai Z, Cerrina F, Chen Z, Gentili M and Gluskin E 1999 *Rev. Sci. Instrum.* **70** 3537
- [71] Yang W, Larson B C, Ice G E, Tischler J Z, Budai J D, Chung K S and Lowe W P 2003 *Appl. Phys. Lett.* **82** 3856
- [72] Larson B C, Yang W, Ice G E, Budai J D and Tischler J Z 2002 *Nature* **415** 887
- [73] MacDowell A A, Celestre R S, Tamura N, Spolenak R, Valek B, Brown W L, Bravman J C, Padmore H A, Batterman B W and Patel J R 2001 *Nucl. Instrum. Methods A* **467–468** 936
- [74] Fischer P, Schutz G, Schmahl G, Guttman P and Raasch D 1996 *Z. Phys. B: Condens. Matter* **101** 313
- [75] Cai Z H *et al* 1999 *Appl. Phys. Lett.* **75** 100
- [76] Cai Z, Lai B, Xiao Y and Xu S 2003 *J. Physique IV* **104** 17
- [77] Kortright J B, Awschalom D D, Stohr J, Bader S D, Idzerda Y U, Parkin S S P, Schuller I K and Siegmann H C 1999 *J. Magn. Magn. Mater.* **207** 7
- [78] Kao C, Hastings J B, Johnson E D, Siddons D P, Smith G C and Prinz G A 1990 *Phys. Rev. Lett.* **65** 373
- [79] MacKay J F, Teichert C, Savage D E and Lagally M G 1996 *Phys. Rev. Lett.* **77** 3925
- [80] Abbamonte P, Blumberg G, Rusydi A, Gozar A, Evans P G, Siegrist T, Venema L, Eisaki H, Isaacs E D and Sawatzky G A 2004 *Nature* **431** 1078
- [81] Schussler-Langeheine C *et al* 2005 *Phys. Rev. Lett.* **95** 156402
- [82] Eisebitt S, Lorgen M, Eberhardt W, Luning J, Stohr J, Rettner C T, Hellwig O, Fullerton E E and Denbeaux G 2003 *Phys. Rev. B* **68** 104419
- [83] Eisebitt S, Luning J, Schlotter W F, Lorgen M, Hellwig O, Eberhardt W and Stohr J 2004 *Nature* **432** 885
- [84] Pierce M S *et al* 2005 *Phys. Rev. Lett.* **94** 017202
- [85] Scholl A *et al* 2000 *Science* **287** 1014
- [86] Stohr J, Scholl A, Regan T J, Anders S, Luning J, Scheinfein M R, Padmore H A and White R L 1999 *Phys. Rev. Lett.* **83** 1862
- [87] Stoll H *et al* 2004 *Appl. Phys. Lett.* **84** 3328
- [88] Vogel J, Kuch W, Bonfim M, Camarero J, Pennec Y, Offi F, Fukumoto K, Kirschner J, Fontaine A and Pizzini S 2003 *Appl. Phys. Lett.* **82** 2299
- [89] Strange P, Durham P J and Gyorffy B L 1991 *Phys. Rev. Lett.* **67** 3590
- [90] Pollmann J, Srajer G, Haskel D, Lang J C, Maser J, Jiang J S and Bader S D 2001 *J. Appl. Phys.* **89** 7165
- [91] Cady A *et al* 2005 *Rev. Sci. Instrum.* **76** 063702
- [92] Yeh A, Soh Y-A, Brooke J, Aeppli G, Rosenbaum T F and Hayden S M 2002 *Nature* **419** 459
- [93] Fawcett E 1988 *Rev. Mod. Phys.* **60** 209
- [94] Braun K F, Folsch S, Meyer G and Rieder K H 2000 *Phys. Rev. Lett.* **85** 3500
- [95] Hopster H 1999 *Phys. Rev. Lett.* **83** 1227
- [96] Kleiber M, Bode M, Ravlic R and Wiesendanger R 2000 *Phys. Rev. Lett.* **85** 4606
- [97] Ravlic R, Bode M, Kubetzka A and Wiesendanger R 2003 *Phys. Rev. B* **67** 174411
- [98] Takahashi M, Igarashi J-I and Hirai K 2004 *Phys. Rev. B* **70** 174441
- [99] Evans P G, Isaacs E D, Aeppli G, Cai Z and Lai B 2002 *Science* **295** 1042
- [100] Hosoya S and Ando M 1971 *Phys. Rev. Lett.* **26** 321
- [101] Ando M and Hosoya S 1972 *Phys. Rev. Lett.* **29** 281
- [102] Davidson J B, Werner S A and Arrott A S 1973 *AIP Conf. Proc.* **18** 396
- [103] Evans P G, Isaacs E D, Aeppli G, Cai Z H and Lai B 2002 *Mater. Res. Soc. Symp. Proc.* **690** F8.6.1
- [104] Barrett C and Massalski T B 1980 *Structure of Metals* (Oxford: Pergamon)
- [105] Pollmann J, Srajer G, Maser J, Lang J C, Nelson C S, Venkataraman C T and Isaacs E D 2000 *Rev. Sci. Instrum.* **71** 2386
- [106] Cooper M J, Zukowski E, Timms D N, Armstrong R, Itoh F, Tanaka Y, Ito M, Kawata H and Bateson R 1993 *Phys. Rev. Lett.* **71** 1095
- [107] Zukowski E, Collins S P, Cooper M J, Timms D N, Itoh F, Sakurai H, Kawata H, Tanaka Y and Malinowski A 1993 *J. Phys.: Condens. Matter* **5** 4077
- [108] Fuess H, Givord D, Gregory A R and Schweizer J 1979 *J. Appl. Phys.* **50** 2000
- [109] Lang J C, Lee D R, Haskel D and Srajer G 2004 *J. Appl. Phys.* **95** 6537
- [110] Gibbs D, Harshman D R, Isaacs E D, McWhan D B, Mills D and Vettier C 1988 *Phys. Rev. Lett.* **61** 1241
- [111] Sutter C, Grubel G, Vettier C, deBergevin F, Stunault A, Gibbs D and Giles C 1997 *Phys. Rev. B* **55** 954
- [112] Kim J W, Kreyssig A, Tan L, Wermeille D, Bud'ko S L, Canfield P C and Goldman A I 2005 *Appl. Phys. Lett.* **87** 202505
- [113] Soh Y-A, Evans P G, Cai Z, Lai B, Kim C Y, Aeppli G, Mathur N D, Blamire M G and Isaacs E D 2002 *J. Appl. Phys.* **91** 7742
- [114] Lottermoser T, Lonkai T, Amann U, Hohlwein D, Ihringer J and Fiebig M 2004 *Nature* **430** 541
- [115] Kimura T, Goto T, Shintani H, Ishizaka K, Arima T and Tokura Y 2003 *Nature* **426** 55
- [116] Bucci J D, Robertson B K and James W J 1972 *J. Appl. Crystallogr.* **5** 187
- [117] Hill N A 2000 *J. Phys. Chem. B* **104** 6694
- [118] Xu G, Hiraka H, Shirane G, Li J, Wang J and Viehland D 2005 *Appl. Phys. Lett.* **86** 182905
- [119] Wang J *et al* 2003 *Science* **299** 1719
- [120] Zavaliche F, Das R R, Kim D M, Eom C B, Yang S Y, Shafer P and Ramesh R 2005 *Appl. Phys. Lett.* **87** 182912
- [121] Eerenstein W, Morrison F D, Dho J, Blamire M G, Scott J F and Mathur N D 2005 *Science* **307** 1203a
- [122] Milward G C, Calderon M J and Littlewood P B 2005 *Nature* **433** 607
- [123] Fiebig M 2005 *J. Phys. D: Appl. Phys.* **38** R123
- [124] Li J H, Levin I, Slutsker J, Provenzano V, Schenck P K, Ramesh R, Ouyang J and Roytburd A L 2005 *Appl. Phys. Lett.* **87**

-
- [125] Zheng H *et al* 2004 *Science* **303** 661
 - [126] Loudon J C, Mathur N D and Midgley P A 2002 *Nature* **420** 797
 - [127] Hellwig O, Berger A and Fullerton E E 2003 *Phys. Rev. Lett.* **91** 197203
 - [128] Ruediger U, Yu J, Zhang S, Kent A D and Parkin S S P 1998 *Phys. Rev. Lett.* **80** 5639
 - [129] Nagy D L *et al* 2002 *Phys. Rev. Lett.* **88** 157202
 - [130] Klein L, Kats Y, Marshall A F, Reiner J W, Geballe T H, Beasley M R and Kapitulnik A 2000 *Phys. Rev. Lett.* **84** 6090
 - [131] Isaac S P, Mathur N D, Evetts J E and Blamire M G 1998 *Appl. Phys. Lett.* **72** 2038
 - [132] Albert F J, Emley N C, Myers E B, Ralph D C and Buhrman R A 2002 *Phys. Rev. Lett.* **89**
 - [133] Albert F J, Katine J A, Buhrman R A and Ralph D C 2000 *Appl. Phys. Lett.* **77** 3809
 - [134] Myers E B, Ralph D C, Katine J A, Louie R N and Buhrman R A 1999 *Science* **285** 867
 - [135] Atkinson D, Allwood D A, Xiong G, Cooke M D, Faulkner C C and Cowburn R P 2003 *Nature Mater.* **2** 85
 - [136] Choi B C, Belov M, Hiebert W K, Ballentine G E and Freeman M R 2001 *Phys. Rev. Lett.* **86** 728
 - [137] Choe S B, Acremann Y, Scholl A, Bauer A, Doran A, Stohr J and Padmore H A 2004 *Science* **304** 420
 - [138] Covington M, Crawford T M and Parker G J 2002 *Phys. Rev. Lett.* **89** 237202
 - [139] Ji Y, Hoffmann A, Jiang J S and Bader S D 2004 *Appl. Phys. Lett.* **85** 6218
 - [140] Tudosa I, Stamm C, Kashuba A B, King F, Siegmann H C, Stohr J, Ju G, Lu B and Weller D 2004 *Nature* **428** 831
 - [141] Vartanyants I A, Robinson I K, Onken J D, Pfeifer M A, Williams G J, Pfeiffer F, Metzger H, Zhong Z and Bauer G 2005 *Phys. Rev. B* **71** 245302